Flow-Dependent Ekman Theory

©Yanxu Chen
Department of Atmospheric and Oceanic Sciences
McGill University
Montreal

Supervised by
Prof. David Straub and Prof. Louis-Philippe Nadeau

A thesis submitted to McGill University in partial fulfilment of the requirements of the degree of M.Sc. in Atmospheric and Oceanic Sciences

Table of Contents

Abstract

Classic Ekman theory predicts a net horizontal transport in the surface boundary layer that is perpendicular to the applied wind stress, and is inversely proportional to the Coriolis parameter, f. This theory, however, neglects feedbacks of the surface currents on the Ekman dynamics and this neglect has led to the development of flow-dependent modifications to the classic theory. The earliest such corrections (Stern 1965 and Niiler 1969) give a transport that is instead inversely proportional to the absolute vertical vorticity, $f + \zeta$. This modification can be justified for plane parallel flows (Niiler 1969) and circular vortices (Stern 1965). Wenegrat and Thomas (2017) recently extend these earlier theories to better account for strong balanced flows with arbitrary curvature. Their method, however, is not easily applicable to complicated flow fields, such as a turbulent ocean saturated with eddies. Here, we first extend the Ekman formulation of Wenegrat and Thomas by adding time dependence. Our new method reproduces transport structures similar to theirs in idealized setting, e.g., for a single balanced vortex. We then couple our flow-dependent Ekman layer to a two-layer shallow water model in which Ekman pumping enters the upper-layer mass equation. The entire system is forced by a combination of steady and high-frequency winds and we compare the kinetic energy response of this Ekman-interior coupled system with that of a standard two-layer model forced by applying the wind stress directly to the upper layer. For low Rossby number flows forced by steady winds, we do not find much difference between the two systems. Adding even a relatively weak high-frequency component to winds, however, leads to significantly different responses at high frequencies between the new and standard models.

La théorie classique d'Ekman prédit un transport horizontal net dans la couche limite de surface qui est perpendiculaire à la contrainte de vent appliquée et est inversement proportionnelle au paramètre de Coriolis, f. Cette théorie, cependant, néglige les rétroactions des courants de surface sur la dynamique d'Ekman et cette négligence a conduit au développement de modifications dépendantes du flux à la théorie classique. Les premières corrections de ce type (Stern 1965 et Niiler 1969) donnent un transport inversement proportionnel au tourbillon vertical absolu, $f + \zeta$. Cette modification peut être justifiée pour les écoulements parallèles plans (Niiler 1969) et les tourbillons circulaires (Stern 1965). Wenegrat et Thomas (2017) ont récemment étendu ces théories antérieures pour mieux tenir compte des flux équilibrés forts avec des courbures arbitraires. Leur méthode, cependant, n'est pas facilement applicable à des champs d'écoulement compliqués, tels qu'un océan turbulent saturé de tourbillons. Ici, nous étendons d'abord la formulation Ekman de Wenegrat et Thomas en ajoutant une dépendance du temps. Notre nouvelle méthode reproduit des structures de transport similaires aux leurs dans un cadre idéalisé, par exemple pour un seul vortex équilibré. Nous couplons ensuite notre couche d'Ekman dépendant du flux à un modèle à deux couches d'eau peu profonde dans lequel le pompage d'Ekman entre dans l'équation de masse de la couche supérieure. L'ensemble du système est forcé par une combinaison de vents constants et de vents haute fréquence et nous comparons la réponse en énergie cinétique de ce système couplé Ekman-intérieur à celle d'un modèle standard à deux couches forcé en appliquant le stress du vent directement sur la couche supérieure. Pour des flux de nombres de Rossby faibles forcés par des vents constants, nous ne trouvons pas beaucoup de différence entre les deux systèmes. L'ajout d'une composante haute fréquence relativement faible aux vents entraîne toutefois des réponses très différentes à haute fréquence entre les nouveaux modèles et les modèles standard.

Acknowledgement

I would first like to thank my thesis advisors Dr. David Straub and Dr. Louis-Philippe Nadeau, for the continuous support of my MSc study and related research, for their patience, motivation and immense knowledge. They consistently allowed this paper to be my own work, but steered me in the right direction whenever they thought I needed it.

I would also like to acknowledge Dr. Carolina Dufour as the thesis examiner and I am gratefully indebted for her valuable comments on this thesis.

Finally, I must express my very profound gratitude to my parents and friends for providing me with unfailing support and continuous encouragement throughout my years of study and through the process of researching and writing this thesis. This accomplishment would not have been possible without them.

Chapter 1

Introduction

The wind sets ocean in motion as a result of its frictional drag on the surface. Intuitively, one expects this force to push a thin layer of water in the same direction as the wind. In a similar manner, this uppermost layer pushes on the layer just below, and so forth. So in other words, one anticipates a vertical structure of the upper ocean with each layer in the same direction of the wind, and with slower speeds further down.

However, if the wind persists, fairly commensurate with the earth's rotation, one must recast the ocean dynamics from a rotating reference frame to describe any flow relative to the moving surface of Earth. And in this frame, a fictitious force (the Coriolis force) drastically modifies the picture above. In this modified picture, the net frictional forcing on each vertical layer is balanced by the Coriolis force. But since the Coriolis force is perpendicular to the current velocity, the uppermost layer responds by deflecting at some angle (to the right in the Northern Hemisphere) relative to the surface wind. Consequently, this layer pushes on the next one down not in the same direction as the wind, but in a direction determined by its motion. Similarly, each layer of water driven by the layer above shifts direction as well and, for an ideal case where a steady horizontal wind blows across an ocean of unlimited depth, a spiral is formed (Figure 1.1). That is, each successive layer moves more towards the right and at a slower speed (Ekman 1905). The range of depths from the surface to the depth at which this spiral velocity becomes negligible is known as the Ekman layer. Typically, the Ekman layer thickness is $\delta \sim O(10^2 m)$, compared with the average ocean depth $D \sim O(10^5 m)$. So the direct effects of the wind are confined to the upper few meters of the ocean. Integrating over the Ekman layer results in a net horizontal transport, which is termed the Ekman transport.

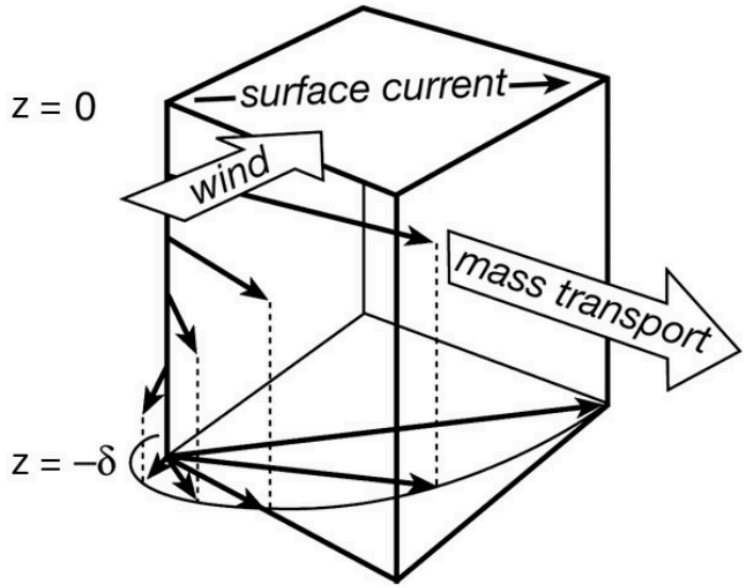

Figure 1.1 The mass transport of the Ekman layer is directed to the right of the wind in the Northern Hemisphere. Horizontal currents within the Ekman layer spiral are shown. (Marshall 2008)

1.1 Development of the Ekman theory

We begin with a brief review of important work related to Ekman dynamics. Classic Ekman theory assumes friction and the Coriolis force to be the only terms in the relevant horizontal balance of forces. This results in a net mass transport that is perpendicular to the wind stress and has a magnitude given by the ratio of the wind stress to the Coriolis parameter, f.

$$\boldsymbol{U}_{Ek} = \frac{\boldsymbol{\tau}\times\hat{\boldsymbol{z}}}{\rho_0 f} \tag{1.1}$$

Here, $\boldsymbol{\tau}$ is surface wind stress and $\boldsymbol{U}_{Ek}$ is the transport integrated over the Ekman layer (with dimensions $\mathrm{m}^2\ \mathrm{s}^{-1}$). And ρ_0 is the density of seawater and we can assume its magnitude to be $\sim 10^3\ \mathrm{kg\ m^{-3}}$ in a simple incompressible fluid context.

Beyond the implications for horizontal flows and transport, spatial variability in the Ekman transport also generates vertical velocities across the base of the Ekman layer. From the perspective of mass conservation, convergent transport drives downward vertical motion (Ekman pumping) and divergent transport drives upward vertical motion from beneath (Ekman suction). In this thesis, "Ekman pumping" is used to represent general effect of both upward and downward motions. We see from Eqn (1.1) that the structure of Ekman transport is determined by the structure of the wind stress and the dependence of f on latitude. For many applications, the latter can be considered small, so that Ekman pumping is dominated by spatial variability of the wind stress. To be more specific, vertical Ekman pumping velocities turn out to be proportional to the wind stress curl. To clarify this, consider the non-divergence constraint integrated over the Ekman layer,

$$\int_{-\delta}^{0} (\frac{\partial u}{\partial x} + \frac{\partial v}{\partial y} + \frac{\partial w}{\partial z}) dz = 0 \tag{1.2}$$

$$\frac{\partial}{\partial x}\int_{-\delta}^{0} u\, dz + \frac{\partial}{\partial y}\int_{-\delta}^{0} v\, dz = -\int_{-\delta}^{0} \frac{\partial w}{\partial z} dz = w(-\delta) = w_{Ek} \tag{1.3}$$

$$w_{Ek} = \frac{\partial}{\partial x}(U_{Ek}) + \frac{\partial}{\partial y}(V_{Ek}) = \frac{\partial}{\partial x}\left(\frac{\tau^y}{\rho_0 f}\right) - \frac{\partial}{\partial y}\left(\frac{\tau^x}{\rho_0 f}\right) = \nabla\times(\frac{\boldsymbol{\tau}}{\rho_0 f}) \tag{1.4}$$

The Ekman pumping velocity, defined by Eqn (1.4), provides a boundary condition for the interior flow that is central to theories of the general ocean circulation (see more details in section 1.2). Figure 1.2 shows a global map of Ekman pumping velocities calculated by Eqn (1.4), linking boundary conditions of the interior ocean to the global wind stress pattern.

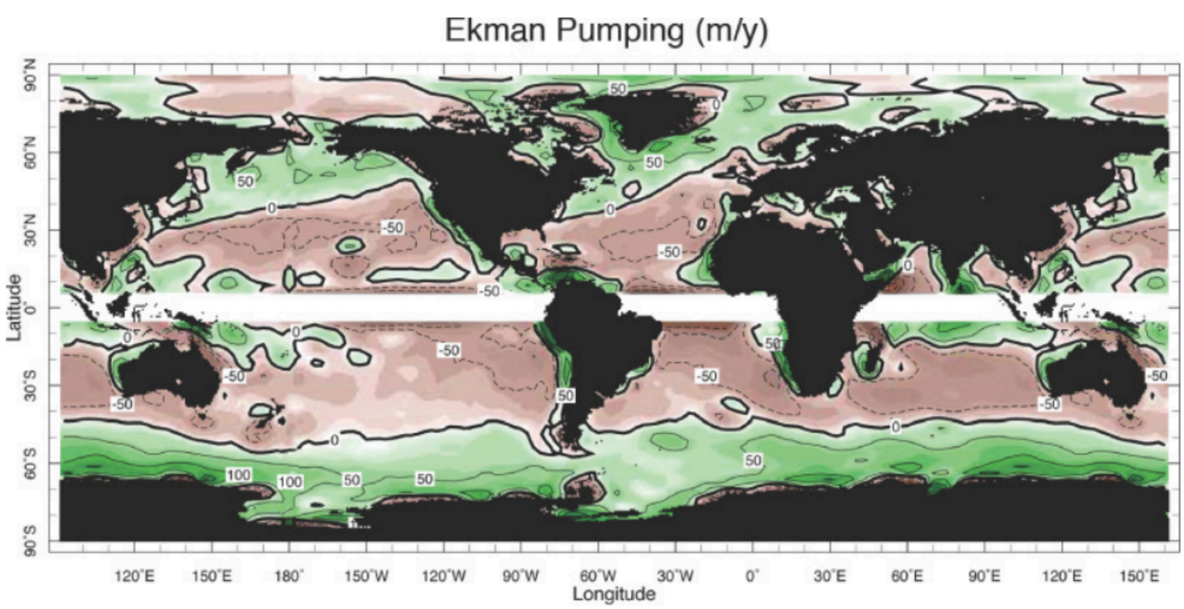

Figure 1.2 The global pattern of Ekman vertical velocity (m y^{-1}) computed using Eqn (1.4) from the annual mean wind-stress pattern. Motion is upward in the green areas, downward in the brown areas. w_{Ek} is not computed over the white strip along the equator because $f \to 0$ there. (Marshall 2008)

Despite the impressive success of classic Ekman theory, it has long been recognized that observations depart significantly from this simple theory. In particular, recent observations have emphasized that synoptic scale winds blowing over ocean eddies and fronts lead to significant vertical pumping (Gaube et al. 2015; Gaube et McGillicuddy 2017; Liu et Tang 2018). This is in large part due to the ocean current and sea surface temperature fields leading to modifications of the wind stress (Trenberth et al 1989; Duhaut et Straub 2006; Zhai et al 2012), but is also in part due to ocean currents modifying the relationship between wind stress and the pumping velocity. Stern (1965) and Niiler (1969) extended the classic theory to include the effects of simple surface currents. In particular, they show Ekman pumping to be modified significantly in currents with strong relative vorticity ($\zeta = \frac{\partial v}{\partial x} - \frac{\partial u}{\partial y}$). These modifications are often referred to as "nonlinear" Ekman theory. The nonlinearity here refers to the influence of surface currents on the Ekman layer but not the self-advection of Ekman velocities. Stern considered a uniform wind stress acting on a geostrophically balanced vortex. There are two velocity scales for the problem: one associated with the balanced flow U and the other with the Ekman flow, $U_E \equiv \frac{\tau_0}{\rho_0 f \delta}$, where τ_0 is a scale for the wind stress and δ indicates Ekman layer thickness. Note that $\boldsymbol{U}_{Ek}$ describes the value of transport integrated over the Ekman layer (with units $\mathrm{m}^2\ \mathrm{s}^{-1}$) while U_E is a typical velocity scale within the Ekman layer (with units $\mathrm{m\ s}^{-1}$). Stern considered flows where the Ekman Rossby number ($\varepsilon_{Ek} = U_E/fL$) and the balanced-flow Rossby number ($\varepsilon = U/fL$) are both much smaller than unity ($\varepsilon_{Ek} \ll 1$ and $\varepsilon \ll 1$). Here, L is a characteristic horizontal length scale. Through scale analysis of the vorticity equation, he showed the Ekman pumping velocity to be given by

$$w_{Ek\_Stern} \approx \nabla \cdot \frac{\boldsymbol{\tau} \times \hat{\boldsymbol{z}}}{\rho_0 (f + \zeta)} \tag{1.5}$$

This solution is notable both for its simplicity and its applicability to flows with curvature. It is noteworthy that contrary to classic Ekman theory, the inclusion of relative vorticity modifies the Ekman pumping velocity such that a horizontally uniform wind stress can nonetheless drive vertical velocities. It is also important to emphasize that Stern's result is correct for calculation of Ekman pumping velocity only, but not the transport (mistakenly used by many people), which means

$$\boldsymbol{U}_{Ek\_Stern} \neq \frac{\boldsymbol{\tau}\times\hat{\boldsymbol{z}}}{\rho_0(f+\zeta)} \tag{1.6}$$

An alternate approach was taken by Niiler (1969), who solved for the horizontal Ekman transport for uniform wind blowing parallel to a straight jet (with strong shear to represent the Gulf Stream). The resulting solutions are accurate to a higher order in ε than those of Stern (1965), and only the nonlinear Ekman self-advection terms in the momentum equations are neglected. The conditions on the validity of Niiler's solution can be given as $\varepsilon_{Ek} \ll 1$ and $\varepsilon < 1$, for a balanced flow that is invariant in one horizontal direction. Considering that Stern's framework does not give an estimate of horizontal transport and that Niiler's framework is limited to plane parallel flows, neither gives a satisfactory way to include surface currents in Ekman dynamics.

More recently, Wenegrat and Thomas (2017) extended earlier results on flow-dependent Ekman dynamics to provide expressions for the Ekman transport that are valid for geostrophically balanced flows with curvature and for flows for which the Rossby number (ε) approaches unity. The latter is especially important in the ocean because many oceanic flows have $\varepsilon \sim 1$, including western boundary currents, flows at low latitude and submesoscale currents, etc. Thus they considered the same limit as Niiler ($\varepsilon_{Ek} \ll 1$ and $\varepsilon < 1$) but without restriction on the flow geometry. This leads to results with much wider applicability than previous methods. To parameterize the position of a streamline of the balanced flow, they switched to a natural coordinate system (see Figure 1.3) from Cartesian coordinate, which seems a useful step in terms of the simplification of dominant equations.

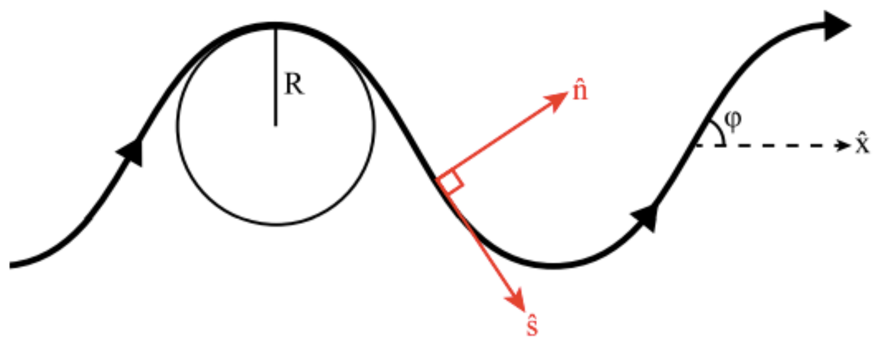

Figure 1.3 Schematic of the balanced natural coordinate system (Wenegrat and Thomas 2017). The black line denotes a streamline of the balanced flow. Red lines denote examples of the locally tangential ($\hat{\boldsymbol{s}}$) and normal ($\hat{\boldsymbol{n}}$) basic vectors, and the vertical dimension ($\hat{\boldsymbol{z}}$) is directed out of the page.

The Ekman transport thus results in two coupled ordinary differential equations in the along-flow coordinate:

$$\varepsilon\bar{u}\frac{\partial U_{Ek}}{\partial s} + (1 + \varepsilon 2\Omega)V_{Ek} = \tau_n \tag{1.7}$$

$$\varepsilon\bar{u}\frac{\partial V_{Ek}}{\partial s} - (1 + \varepsilon\zeta)U_{Ek} = \tau_s \tag{1.8}$$

where $\bar{u}$ is the magnitude of balanced flow velocity, $\Omega \equiv \bar{u}k$ is the angular velocity, $\zeta \equiv -\frac{\partial \bar{u}}{\partial n} + \Omega$ is the relative vorticity, $(\tau_s, \tau_n) = (\boldsymbol{\tau} \cdot \hat{\boldsymbol{s}}, \boldsymbol{\tau} \cdot \hat{\boldsymbol{n}})$, and $k \equiv \left(\frac{\partial \hat{s}}{\partial s}\right) \cdot \hat{\boldsymbol{n}} = 1/R$ with R as the radius of the local osculating circule, defines as a positive value (negative) when streamlines curve to the left (right) of the local balanced flow (see Figure 1.3).

The solutions of the coupled ODEs in Wenegrat and Thomas's theory can be found analytically if the balanced flow has simple structures, e.g., a circular vortex or a weakly nonlinear jet. However, it would be difficult to apply their equations to complicated (balanced or unbalanced) background flow fields, e.g., jets with random shapes, turbulent eddies, etc. Motivated by applying flow-dependent Ekman dynamics to flows with arbitrary curvature more efficiently, we extend Wenegrat and Thomas's formulation by adding a time dependence. This step removes the need for integrating along streamlines, which also means the coordinate switch is not necessary, further simplifying the calculation and enabling our situation to be applied to complicated flow fields. The addition of unsteady terms in our formulation also introduces a near-inertial component to the Ekman pumping (details in section 1.3 and 2.1).

Table 1.1 Summary of the Ekman theory development

	Ekman	Stern and Niiler	Wenegrat and Thomas
Content	Transport depends on the stress and the Coriolis parameter only.	Allows for shear in the surface velocity field to affect the transport: "nonlinear" Ekman theory.	Extends early results to better account for curvature in the surface flow path.

Assumptions	Homogeneous deep stationary ocean.	Valid for plane parallel flows (e.g., straight jets); however, not explicitly solved for flows with curvature.	Curvilinear flows, with $\varepsilon_{Ek} \ll 1$ and $\varepsilon < 1$; however, not easily applicable to complicated flow fields.

1.2 Response of the interior ocean to Ekman pumping

Beneath the Ekman layer, the flow can be thought of as a superposition of geostrophic flow and inertia-gravity waves. Classic theory has focused on how Ekman pumping velocity interacts with the geostrophic currents. Taking the horizontal divergence of the geostrophic flow, we find:

$$\nabla_h \cdot \boldsymbol{u}_g = \frac{\partial}{\partial x}\left(-\frac{1}{\rho_0 f}\frac{\partial p}{\partial y}\right) + \frac{\partial}{\partial y}\left(\frac{1}{\rho_0 f}\frac{\partial p}{\partial x}\right) = -\frac{\beta}{f} v_g \tag{1.9}$$

where we consider the variation of f with latitude and the meridional gradient of f is denoted by β. Then the resulting horizontal divergence of geostrophic flow is associated with vertical stretching of water columns:

$$\nabla_h \cdot \boldsymbol{u}_g + \frac{\partial w}{\partial z} = 0 \tag{1.10}$$

Combining Eqns (1.9) and (1.10) we obtain an expression for the interior geostrophic flow:

$$\beta v_g = f \frac{\partial w}{\partial z} \tag{1.11}$$

which relates horizontal and vertical currents. If vertical velocity magnitude in the abyss is much smaller than surface Ekman pumping velocities, then interior ocean currents will have a southward component in regions where $w_{Ek} < 0$ and northward where $w_{Ek} > 0$ (Figure 1.4).

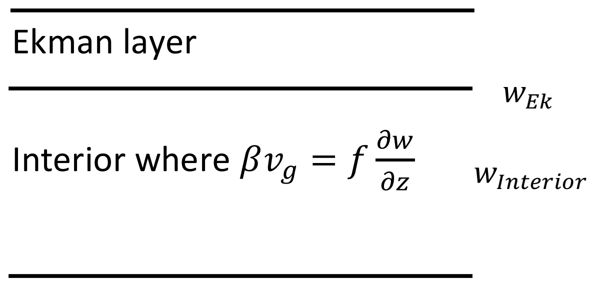

Figure 1.4 Classic Ekman-interior coupled model

By integrating Eqn (1.11) from the bottom of Ekman layer to a depth of no motion (e.g., 1000m), we can obtain a Sverdrup balance (1947), which is the first model of general ocean circulation. In 1948, Stommel used the same basic equations but integrated to the bottom of the ocean and allowed for bottom friction which is a simple linear function of velocity, and the results showed that the variation in Coriolis parameter with latitude leads to a narrow western boundary current in ocean basins. Munk (1950) proposed a complete solution for the ocean circulation, by further adding a lateral eddy diffusion term associated with the horizontal exchange of large eddies. In summary, Ekman pumping velocity sets a boundary condition for the interior ocean circulation.

However, the classic general ocean circulation theory has focused on the response of geostrophically balanced interior flow to simple Ekman layer framework. Here, we instead assume the interior flow to be a superposition of geostrophic flow and inertia-gravity waves, and then our interest is to answer how the new framework of flow-dependent Ekman layer affects the interior response both geostrophically and ageostrophically. To this end, we will embed our flow-dependent Ekman layer into a two-layer shallow water model and compare solutions when the model is forced by Ekman pumping with solutions where wind forcing takes a more typical form of a body force applied over the upper layer.

1.3 Consideration of high-frequency components in the Ekman framework

As mentioned earlier, the ocean contains not only geostrophic (balanced) currents and eddies, but also high-frequency (unbalanced) oscillations that exist under various circumstances. However, models based on Ekman theory are mainly aimed at the response of geostrophic components to the Ekman pumping velocities. Simple shallow water models that look at both balanced currents and waves generally represent the wind stress as a body force, instead of adding an extra Ekman framework (Figure 1.5 left). General circulation models, of course, explicitly resolve the Ekman layer, but our interest here is to relate Ekman theory to the interior flow in simple ways and to compare different dynamical regimes specifically by using certain wind stress structures.

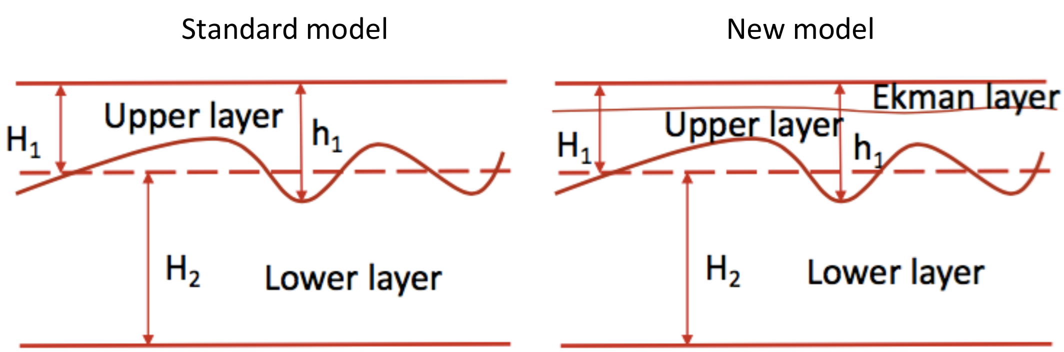

Figure 1.5 Typical ocean models forced by wind (Left: A two-layer shallow-water model with the wind stress as a body force over the upper layer (later we call it the **standard model**); Right: A model with the Ekman layer as a link transferring momentum from wind to deep ocean (later we call it the **new model**))

The main purpose of this thesis is to compare the above two models in Figure 1.5 with the focus on how advanced or dynamically different the Ekman-interior coupled model is. There are two important interfaces in the Ekman-interior coupled model associated with high-frequency energy transfer: the interface between wind and the Ekman layer, and the interface between Ekman layer and the upper layer.

In the first place, it is important to look at the wind stress structure. The wind stress over ocean surface can be modelled by the bulk formula, which depends quadratically on the wind:

$$\boldsymbol{\tau} = \rho_a C_d |\boldsymbol{U}_{wind}| \boldsymbol{U}_{wind} \tag{1.12}$$

where $\boldsymbol{U}_{wind}$ is the wind velocity above the sea surface; ρ_a is the density of air at sea level and C_d is the drag coefficient. Classic models of ocean circulation focus on steady solutions and low-frequency variability. These models often assume steady or slowly varying winds. Although this may be true in regions where there is little wind variability, it breaks down in regions where the synoptic wind dominates: for example, the storm-track regions (Zhai et al 2012). This is because high-frequency winds not only contribute to the time-averaged (or low-frequency) wind stress, but also introduce high frequencies in the stress itself. Figure 1.6 shows the variability of global wind stress curl. Remind us that Ekman pumping is mainly determined by wind stress curl. Then the difference between January and July in Figure 1.6 tells that the wind stress curl is more variable at mid-to-high latitudes and thus the high-frequency curl components of the stress might be more contributing to Ekman pumping at those areas. Back to our study of the new Ekman-interior coupled framework, we are therefore interested in studying how the Ekman dynamics responds to high-frequency components of wind stress.

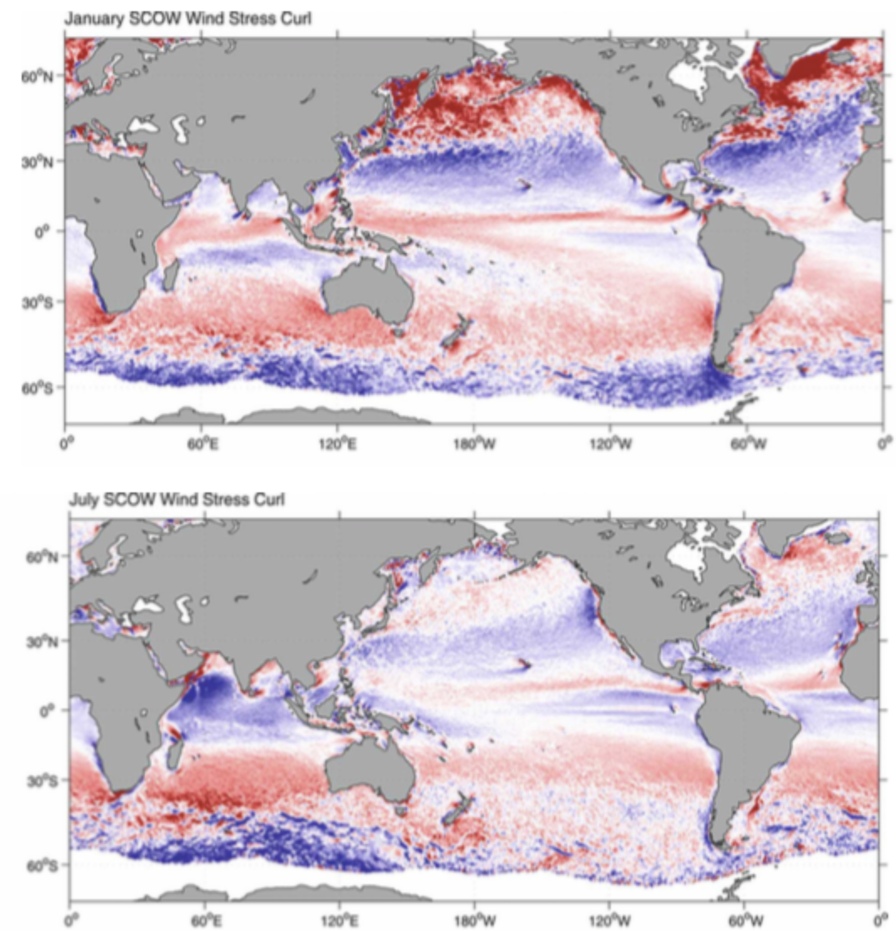

Figure 1.6 Global Scatterometer Climatology of Ocean Winds (SCOW) wind stress curl maps for (upper) January and (lower) July (Risien et al, 2008)

Another important consideration is the high-frequency energy transfer between the Ekman layer and the interior ocean. Ekman pumping velocities calculated using high-frequency components of wind stress might also induce some high frequencies, continuously influencing the interior in a different way compared with the mechanism where the interior ocean is driven by time-averaged Ekman pumping.

From observations we know that it is more reasonable to apply time-dependent wind stress to the ocean. By modifying Wenegrat and Thomas's Ekman transport formulation, we also allow for time dependence in the Ekman pumping. Thus, we are interested in testing whether the addition of a flow-dependent Ekman layer can be used as an alternative way to implement wind forcing in a two-layer shallow water model and how different this mechanism is from a standard model in terms of the high-frequency energy transfer.

1.4 Ocean eddies and the flow-dependent Ekman theory

Mesoscale eddies and geostrophic turbulence are ubiquitous in the ocean and exhibit different properties to their surroundings, allowing them to transport properties such as heat, salt and carbon around the ocean. More than half of the kinetic energy of the ocean circulation is contained in the mesoscale eddy field, with the remainder largely contained in the large-scale circulation. The largest-scale eddies emerge from instabilities of strongly horizontally sheared motions, particularly in boundary currents such as the Gulf Stream. These eddies often take the form of well-defined rings extending to great depth. At slightly smaller scales, on the order of tens of kilometers (mesoscale), eddies are generated by baroclinic instability.

As mentioned before, previous flow-dependent Ekman theory is not applicable to the real ocean, which includes abundant, turbulent eddies. Theories by Stern and Niiler are too simple and while that by Wenegrat and Thomas could in principle be applied to an eddy-rich field, the calculation would be horrendous. Our research interest is greatly related to the understanding of how ocean "storms", or mesoscale eddies, help to modify the Ekman dynamics and then how this flow-dependent Ekman layer changes the interior response as well. Note that one could also ask these questions using a general circulation model that explicitly resolves the surface Ekman layer. We believe, however, that it is also useful to examine these issues in a more idealized context, such as that developed in this thesis.

Chapter 2

Numerical model

2.1 The Ekman model
2.1.1 Governing equations

Consider an Ekman layer superposed on a background eddying flow with a velocity $\boldsymbol{u}_0$. The total horizontal flow can be written as $\boldsymbol{u}_{total} = \boldsymbol{u}_0 + \boldsymbol{u}_{Ek}$, where $\boldsymbol{u}_{Ek}$ is the wind-forced Ekman component. It is further assumed that the background flow is either barotropic or the Ekman layer is sufficiently thin so as to allow the background flow to be approximated as barotropic, i.e., $\delta \ll H$, where H is the depth scale of the balanced flow. We are interested in finding solutions for the Ekman flow in the presence of a steady, spatially uniform, wind stress. The variables can thus be nondimensionalized as follows: $u_0 = U_0 u_0'$, $(u_{Ek}, v_{Ek}, w_{Ek}) = U_E[u_{Ek}', v_{Ek}', (\delta/L)w_{Ek}']$, $(\tau^x, \tau^y) = \tau_0(\tau^{x\prime}, \tau^{y\prime})$, $x = Lx'$, $y = Ly'$, $z = \delta z'$, $\mathrm{t} = Tt'$, where primes denote nondimensional variables. The equations governing the horizontal Ekman flow can be written in vector form as

$$\frac{\partial \boldsymbol{u}_{Ek}}{\partial t} + (\boldsymbol{u}_{Ek} \cdot \nabla)\boldsymbol{u}_0 + (\boldsymbol{u}_0 \cdot \nabla)\boldsymbol{u}_{Ek} + (\boldsymbol{u}_{Ek} \cdot \nabla)\boldsymbol{u}_{Ek} + f\hat{\boldsymbol{z}}\times\boldsymbol{u}_{Ek} = \frac{\partial \boldsymbol{\tau}}{\partial z} \quad (2.1)$$

Using scalings, we can write a nondimensionalized equation

$$\frac{1}{fT}\frac{\partial \boldsymbol{u}_{Ek}'}{\partial t'} + \varepsilon \boldsymbol{u}_{Ek}' \cdot \nabla \boldsymbol{u}_0' + \varepsilon \frac{\alpha U_E}{U_E} \boldsymbol{u}_0' \cdot \nabla \boldsymbol{u}_{Ek}' + \varepsilon_{Ek} \frac{\alpha U_E}{U_E} \boldsymbol{u}_{Ek}' \cdot \nabla \boldsymbol{u}_{Ek}' + \hat{\boldsymbol{z}}\times\boldsymbol{u}_{Ek}' = \frac{\partial \boldsymbol{\tau}'}{\partial z'} \quad (2.2)$$

where the gradient in Ekman flow is scaled as $\nabla \boldsymbol{u}_{Ek} \sim \alpha U_E/L$. For a spatially uniform wind stress $\alpha U_E/U_E \sim \varepsilon$ (Stern 1965); hence, the third and fourth terms on the left-hand side appear at $O(\varepsilon^2)$ and $O(\varepsilon_{Ek}\varepsilon)$, respectively.

If we consider the limit of Wenegrat and Thomas's formulation ($\varepsilon_{Ek} \ll 1$ and $\varepsilon < 1$), the fourth term on the left-hand side, which is the Ekman self-advection term, can be neglected. If so, integrating Eqn (2.1) over the entire Ekman layer results in an equation for the Ekman transport,

$$\frac{\partial \boldsymbol{U}_{Ek}}{\partial t} + (\boldsymbol{U}_{Ek} \cdot \nabla)\boldsymbol{u}_0 + (\boldsymbol{u}_0 \cdot \nabla)\boldsymbol{U}_{Ek} + f\hat{\boldsymbol{z}}\times\boldsymbol{U}_{Ek} = \boldsymbol{\tau} \tag{2.3}$$

The time-dependent term, which is the first term on the left-hand side, does not appear in Wenegrat and Thomas's formulation and is added here as a convenience to avoid having to integrate along characteristics to recover $\boldsymbol{U}_{Ek}$. Note, however, that the addition of this term also allows for high-frequency oscillations in $\boldsymbol{U}_{Ek}$, irrespective of whether or not there are high frequencies in $\boldsymbol{\tau}$. The Ekman pumping velocity, w_{Ek}, can be found by taking the horizontal divergence of Eqn (2.3). By taking the high-frequency components of $\boldsymbol{U}_{Ek}$ into consideration, the Ekman pumping velocity then contains high frequencies and thus further triggers similar response of the interior. It is also noteworthy that the units for $\boldsymbol{U}_{Ek}$ are $\mathrm{m}^2\ \mathrm{s}^{-1}$ while $\boldsymbol{u}_0$ has the dimension of $\mathrm{m\ s}^{-1}$. Compared with previous section, notation henceforth is simplified in that $\boldsymbol{\tau}$ has been normalized by ρ_0.

2.1.2 Verification: using a single vortex case

Wenegrat and Thomas considered a purely zonal wind stress over a circular vortex and found that there can be a nonzero component of the Ekman transport in the direction of the zonal wind stress, which is contrary to classical Ekman theory. An illustration is shown in Figure 2.1. The zonal transport develops a quadrupole patter, emphasizing the influence of the flow-dependent Ekman dynamics. The meridional transport converges (diverges) on the north (south) side of the cyclonic vortex, with the pattern reversed for the vortex with anticyclonic flow and with slight differences in structure between the two cases.

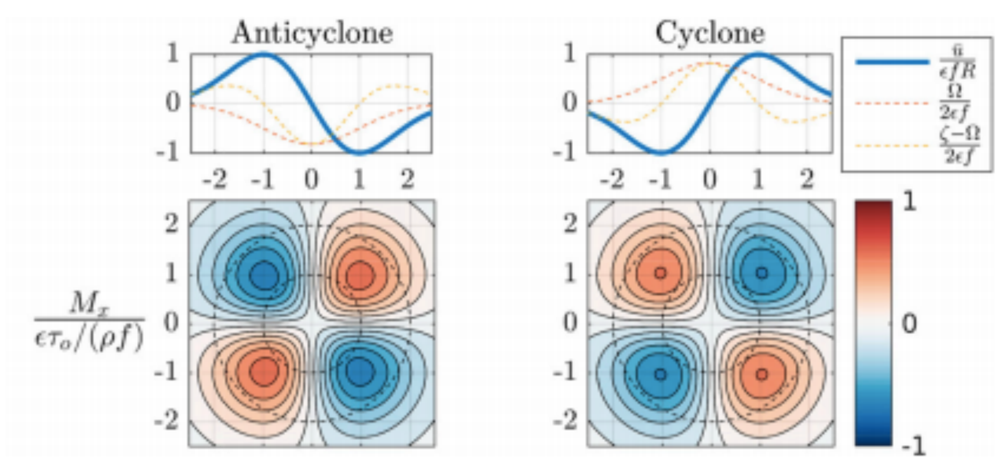

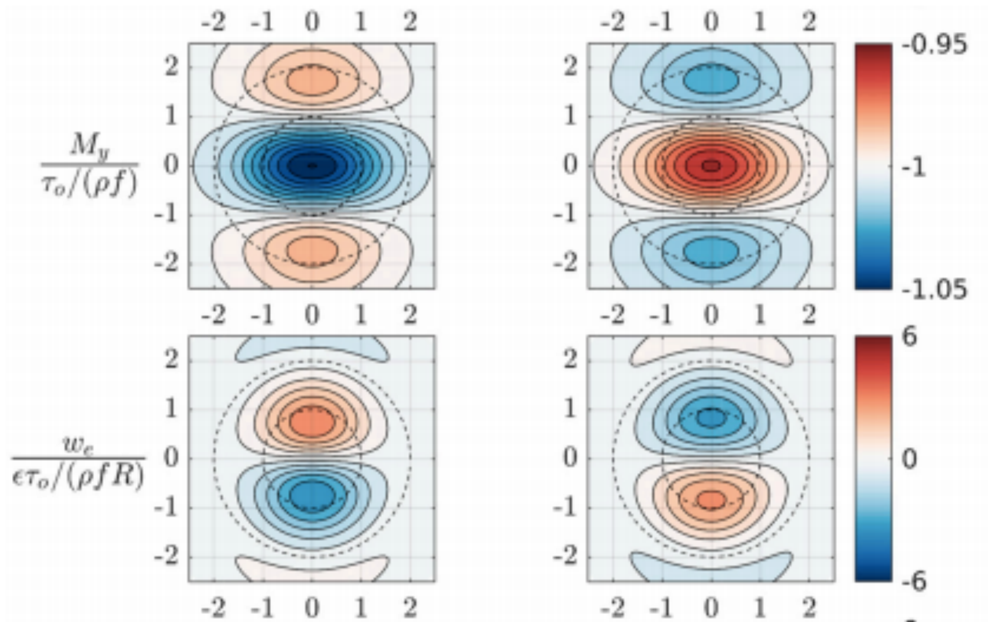

Figure 2.1: Ekman transports and vertical velocities in Wenegrat and Thomas model. From top to bottom, the rows show zonal transport U_{Ek}, meridional transport V_{Ek} and vertical velocity w_{Ek}. (Wenegrat and Thomas 2017)

As a consistency check, we begin by reproducing the above results with our model. That is, we apply a uniform westerly wind stress over a circular eddy. To minimize transients (the high-frequency oscillations of $\boldsymbol{U}_{Ek}$, which is described in section 2.1.1), we ramp up the wind stress slowly (over ten inertial periods). The eddy structure is also consistent with Wenegrat and Thomas's vortex, with parameters chosen such that the transport magnitude $|U_{Ek}|{\sim}1.5\ \mathrm{m^2\ s^{-1}}$ (using $\tau{\sim}10^{-4}\ \mathrm{m^2\ s^{-2}}$, $f{\sim}7\cdot10^{-5}\ \mathrm{s^{-1}}$, $\varepsilon{\sim}0.25$), in accordance with the observed global-mean properties of midlatitude mesoscale eddies.

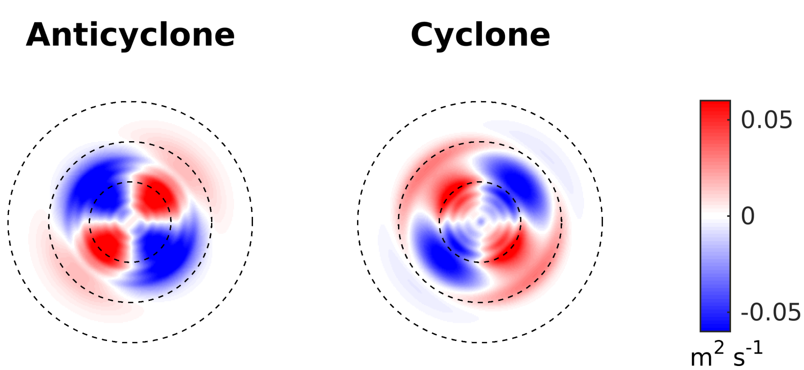

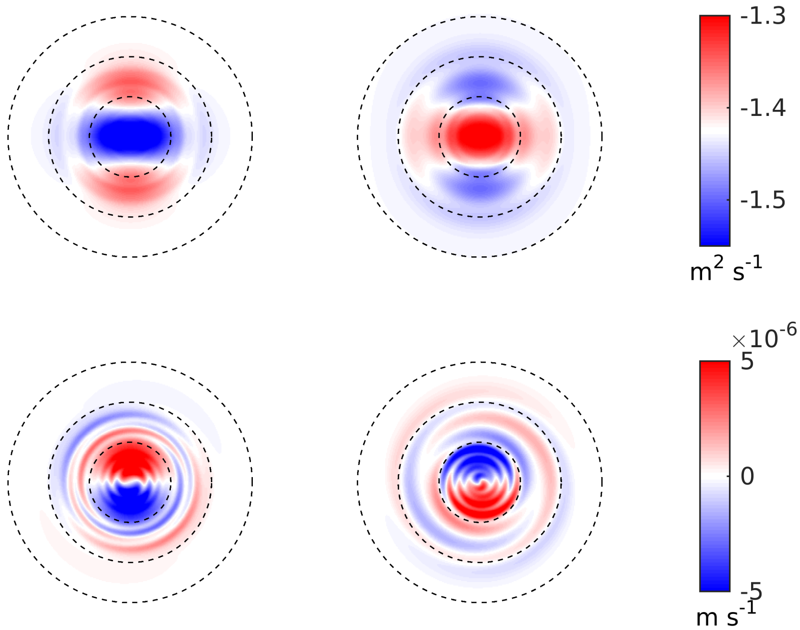

Figure 2.2: Ekman transports and vertical velocities for a circular vortex forced by a westerly wind stress. From top to bottom, the rows show zonal transport U_{Ek}, meridional transport V_{Ek} and vertical velocity w_{Ek}.

Our results correspond well with Wenegrat and Thomas's analytic solutions (compare Figure 2.1 and Figure 2.2). Figure 2.2 is a snapshot of our Ekman model output. However, our model produces transients even though the wind forcing is switched on with extremely slow speed, e.g., over one month. Figure 2.3 illustrates how robust the transient part is. The transient pumping component decreases when the time period to entirely switch on the wind stress is increased, however, it cannot be eliminated. This new framework of adding high-frequency transients helps to test the interior response to high-frequency Ekman pumping (details in section 3).

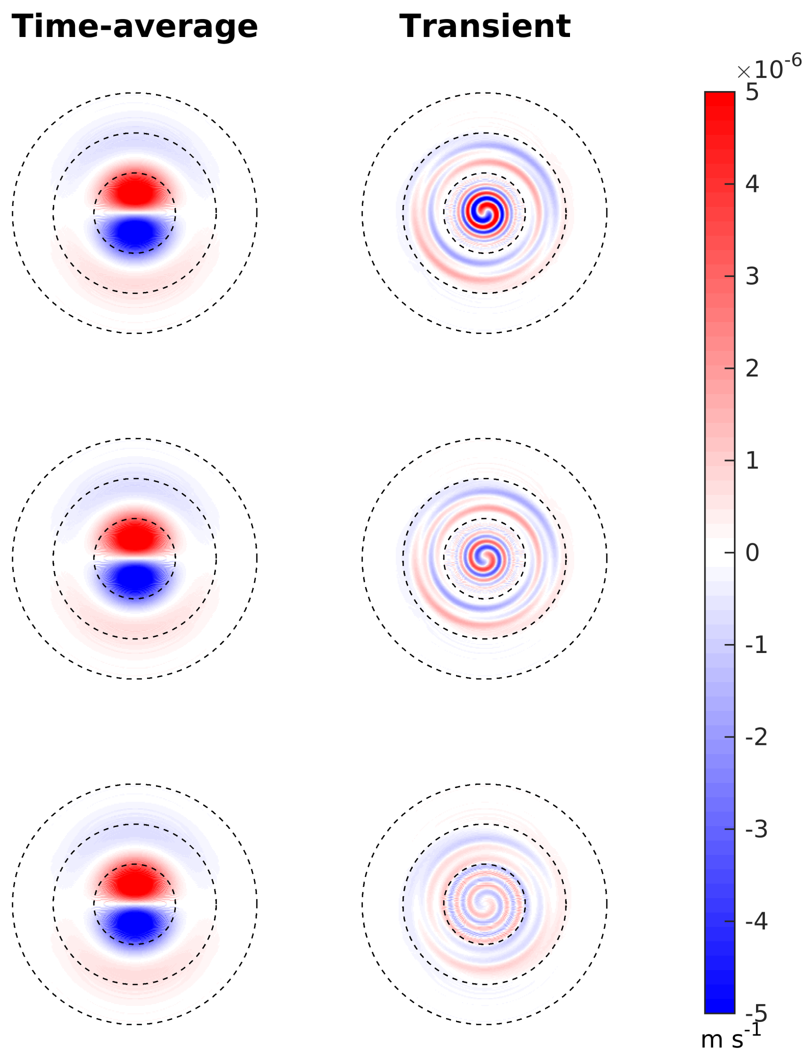

Figure 2.3: Ekman pumping velocities for an anticyclonic vortex forced by a westerly wind stress, decomposed into a time-averaged part and a transient part. The time period to fully ramp up the wind stress is denoted by the number of inertial periods n. From top to bottom, $n = 1, 5, 30$.

Figure 2.4 shows the ratio of transient kinetic energy to mean kinetic energy in the Ekman layer. It is apparent that transients decrease as more inertial periods are used to entirely turn on the wind. That means in order to avoid the influence of transients in the Ekman layer, we need to use a reasonable ramp-up time to slowly switch on the wind stress.

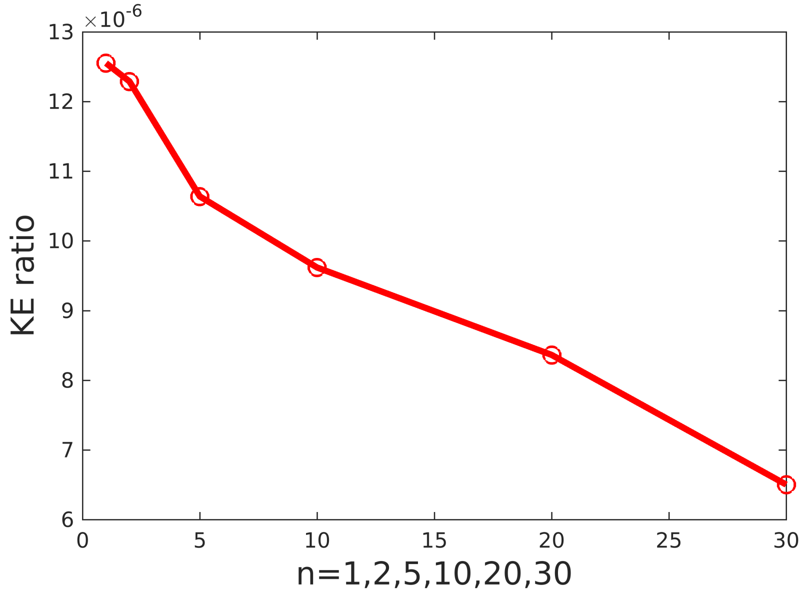

Figure 2.4 The ratio of transient kinetic energy to mean kinetic energy in the Ekman layer, as a function of how many inertial periods (n) is used to turn on the wind.

2.2 The two-layer shallow water model

2.2.1 A typical two-layer shallow water system

The case of two superposed shallow layers of different density is always regarded as a simple starting point for understanding the behavior of vertically stratified flow. "Shallow" here means that the depth of each layer is small compared with the horizontal scale of perturbation. The setup of the system to be considered is shown in Figure 2.5. It has a lower layer of density ρ_2 and an upper layer of density ρ_1, where $\rho_1 < \rho_2$. The free surface, whose equilibrium position is $z = 0$, has perturbed position $z = \eta_1$ and the interface displacement has the position $z = \eta_2$. It is assumed that hydrostatic balance applies and the pressure varies continuously across the interface between the two layers but the density does not. Therefore, the shallow water momentum equations are

$$\frac{D\boldsymbol{v}_1}{Dt} + f\hat{\boldsymbol{z}}\times\boldsymbol{v}_1 = -g\nabla\eta_1 \qquad (2.4a)$$

$$\frac{D\boldsymbol{v}_2}{Dt} + f\hat{\boldsymbol{z}}\times\boldsymbol{v}_2 = -\frac{\rho_1}{\rho_2}g\nabla\eta_1 - g'\nabla\eta_2 \approx -g\nabla\eta_1 - g'\nabla\eta_2 \qquad (2.4b)$$

where g' is the reduced gravity, defined by

$$g' = \frac{g(\rho_2 - \rho_1)}{\rho_2} \quad (2.5)$$

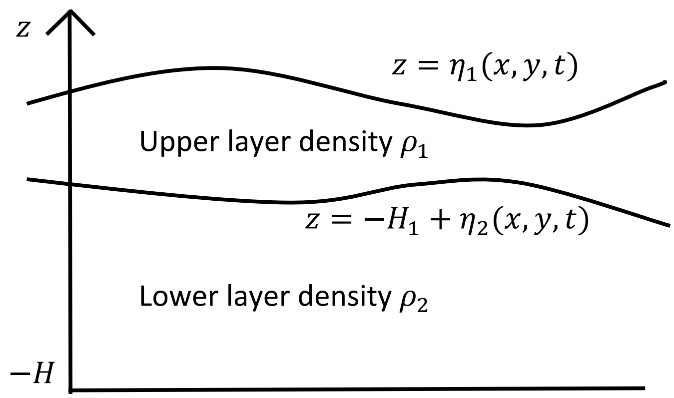

Figure 2.5 The notation used to describe the motion of two superposed shallow homogeneous layers of fluid. H_1, H_2 are the depths of the layers when at rest and $H = H_1 + H_2$ is the total depth. The z axis points vertically upward, $z = \eta_1(x, y, t)$ is the surface elevation, and $z = -H + \eta_2(x, y, t)$ gives the disturbed position of the interface between the two fluids. The thicknesses of the layers are $h_1 = H_1 + \eta_1 - \eta_2$ and $h_2 = H_2 + \eta_2$ respectively.

whereas the continuity equations are

$$\frac{Dh_1}{Dt} + h_1\left(\frac{\partial u_1}{\partial x} + \frac{\partial v_1}{\partial y}\right) = 0 \quad (2.6a)$$

$$\frac{Dh_2}{Dt} + h_2\left(\frac{\partial u_2}{\partial x} + \frac{\partial v_2}{\partial y}\right) = 0 \quad (2.6b)$$

2.2.2 The baroclinic mode and the rigid lid approximation

The disparity in the values of g' and g means that approximations can be made to the equations and boundary conditions, depending on the mode being studied. Following Gill (1982), we can describe the flow with two independent vertical modes, called the barotropic (sum of the two layers) and baroclinic (difference of the two layers) modes. For the barotropic mode, the approximation is simply to ignore density differences altogether and treat fluid as one of uniform density.

And there are two approximations used to obtain the baroclinic mode. The first uses the fact that for this mode surface displacements are small compared with interface displacements. Thus the continuity equation (2.6a) is approximated by

$$-\frac{\partial \eta_2}{\partial t} + (\boldsymbol{v}_1 \cdot \nabla)(\eta_1 - \eta_2) + h_1\left(\frac{\partial u_1}{\partial x} + \frac{\partial v_1}{\partial y}\right) = 0 \qquad (2.6a\_new)$$

where $h_1 = H_1 - \eta_2$.

The momentum equations for the upper layer are given by (2.4a) as before. This is called the rigid lid approximation, although the name is misleading because free surface displacements are required to give pressure gradients in the upper layer (i.e., (2.4a) involves $\nabla\eta_1$). The justification for the name lies in the fact that if there were a rigid lid at $z = 0$, the identical pressure gradients would be achieved because the rigid lid would provide the necessary pressure. The second approximation is simply to replace the ratio ρ_1/ρ_2 by unity, as shown in (2.4b). This is usually referred to as the Boussinesq approximation that the differences in inertia of the two layers is negligible but their weights are different. Equations (2.4) and (2.6b) usually compose a typical rigid lid two-layer shallow water system.

We can define our baroclinic and barotropic velocities as follows:

$$\boldsymbol{v}_{bc} = \boldsymbol{v}_2 - \boldsymbol{v}_1 \qquad (2.7)$$

$$\boldsymbol{v}_{bt} = \frac{H_1\boldsymbol{v}_1 + H_2\boldsymbol{v}_2}{H} \qquad (2.8)$$

$\boldsymbol{v}_{bc}$ and $\boldsymbol{v}_{bt}$ can also be thought of as the amplitude of the baroclinic mode and barotropic mode respectively. And then we can rewrite the shallow water equation system with baroclinic and barotropic velocities.

$$\frac{\partial \boldsymbol{v}_{bc}}{\partial t} + (\boldsymbol{v}_{bt} \cdot \nabla)\boldsymbol{v}_{bc} + (\boldsymbol{v}_{bc} \cdot \nabla)\boldsymbol{v}_{bt} + f\hat{\boldsymbol{z}}\times\boldsymbol{v}_{bc} = -g'\nabla\eta_2 \qquad (2.9)$$

$$\frac{\partial \boldsymbol{v}_{bt}}{\partial t} + \frac{H_1}{H}(\boldsymbol{v}_{bt} \cdot \nabla)\boldsymbol{v}_{bt} + \frac{H_1^2 H_2}{H^3}(\boldsymbol{v}_{bc} \cdot \nabla)\boldsymbol{v}_{bc} + f\hat{\boldsymbol{z}}\times\boldsymbol{v}_{bt} = -g\nabla\eta_1 - g'\frac{H_2}{H}\nabla\eta_2 \qquad (2.10)$$

$$\frac{\partial \eta_2}{\partial t} = -(H_2 + \eta_2)\nabla \cdot \left(\boldsymbol{v}_{bt} - \frac{H_2}{H}\boldsymbol{v}_{bc}\right) - \left(\boldsymbol{v}_{bt} - \frac{H_2}{H}\boldsymbol{v}_{bc}\right) \cdot \nabla \eta_2 \quad (2.11)$$

Waves traveling on barotropic and baroclinic modes have specific phase speeds:

$$c_{bt} = \sqrt{gH} \approx 200 \text{ m } s^{-1} \quad (2.12)$$

$$c_{bc} = \sqrt{g' H_e} \approx 2 \text{ m } s^{-1} \quad (2.13)$$

where $H_e = H_1 H_2 / H$, is the equivalent height. Here, we apply $H = 4000$ m, $H_1 = 1000$ m and $H_2 = 3000$ m in our model. After making the rigid lid approximation, the barotropic gravity waves no longer exist, which means that c_{bt} is replaced with an infinite gravity wave speed and $\eta_1 = 0$ in our model.

2.2.3 Decomposition into quasigeostrophic and ageostrophic parts

Quasigeostrophy assumes the Rossby and Froude numbers to be small. Equivalently, it is assumed that $\varepsilon \sim \varepsilon (\frac{L}{L_d})^2 \ll 1$, where the deformation radius L_d is defined as

$$L_d^2 \equiv \frac{g' H_e}{f^2} = \frac{c_{bc}^2}{f^2} \quad (2.14)$$

From the perspective of potential vorticity, we can also define barotropic and baroclinic potential vorticity to describe the two-layer quasigeostrophic (QG) system.

$$q_{bt} = \frac{H_1 \zeta_1 + H_2 \zeta_2}{H} \quad (2.15)$$

$$q_{bc} = \zeta_2 - \zeta_1 - \frac{f \eta_2}{H_e} \quad (2.16)$$

Since the potential vorticity is a Laplacian-like operator of the stream function ψ and the QG potential vorticity is conserved, each q mode mentioned above can be solved and results in two ψ modes by doing the inverse Laplacian transformation. To be specific,

$$\frac{Dq}{Dt} = 0 \tag{2.17}$$

where q can be either q_{bt} or q_{bc}.

$$q_{bt} = \nabla^2 \psi_{bt} \tag{2.18}$$

$$q_{bc} = \nabla^2 \psi_{bc} - \frac{1}{L_d^2} \psi_{bc} \tag{2.19}$$

Knowing the value of ψ_{bt} and ψ_{bc} and given the definition of stream function, QG velocities of both layers are also easy to achieve. Next, the ageostrophic (AG) part of velocities is simply the difference between the total and the QG part.

Typically, the QG (or geostrophic) part of the total flow contains most of the slow motion and the ageostrophic part is dominated by fast time scale motion, such as inertia-gravity or Poincaré waves. Later, we will use this decomposition of the flow to interpret our results.

2.2.4 Coupling of the Ekman model and the two-layer shallow water model

As described in section 1 (Figure 1.4), we compare a typical two-layer shallow water model using the wind stress as a body force of the upper layer momentum equation with our new model where the flow-dependent Ekman pumping enters the upper layer mass equation. Here, we assume a zonal wind stress as a cosine function of latitude.

Consider the momentum and mass equations of the upper layer using **standard method**

$$\frac{\partial}{\partial t}\boldsymbol{u}_1 + (\boldsymbol{u}_1 \cdot \nabla)\boldsymbol{u}_1 + f\hat{z}\times\boldsymbol{u}_1 = -g\nabla\eta_1 + \frac{\boldsymbol{\tau}}{h_1} \tag{2.20}$$

$$\frac{\partial}{\partial t}h_1 + \nabla \cdot (h_1\boldsymbol{u}_1) = 0 \tag{2.21}$$

Governing equations for the lower layer are similar to equations described in section 2.2.1. The **new method** to represent wind forcing applies an explicit Ekman layer with dynamics described by Eqn (2.3) and then this flow-dependent Ekman pumping enters as a forcing term in the mass continuity equation

$$\frac{\partial}{\partial t}\boldsymbol{u}_1 + (\boldsymbol{u}_1 \cdot \nabla)\boldsymbol{u}_1 + f\hat{z}\times\boldsymbol{u}_1 = -g\nabla\eta_1 \tag{2.22}$$

$$\frac{\partial}{\partial t}h_1 + \nabla \cdot (h_1\boldsymbol{u}_1) = -w_{Ek} \tag{2.23}$$

To recap, the focus of this thesis is to compare the standard two-layer model (Eqn (2.20) and (2.21)) with a new Ekman-interior coupled model (Eqn (2.22) and (2.23)). Later in all figures, "standard" denotes the typical two-layer model with wind as the body force and "new" represents our Ekman-interior coupled system.

2.2.5 Wind forcing structure and model parameters

The two-layer shallow water system described above is forced by a steady westerly wind stress that varies sinusoidally in y-direction.

$$\tau^x = \tau_0 \cdot \cos\left(\frac{2\pi y}{L_y}\right) \tag{2.24a}$$

$$\tau^y = 0 \tag{2.24b}$$

where $\tau_0 = 2 \cdot 10^{-4}\ \mathrm{m^2\ s^{-2}}$ and the domain size is characterized by $L_y = L_x = 2000\ \mathrm{km}$. Table 2.1 below indicates other parameters in the model.

Table 2.1 Parameters in the two-layer shallow water model

Parameters	Values
Resolution (grid points)	$n_x = n_y = 512$
Coriolis parameter	$f = 7 \cdot 10^{-5}\ \mathrm{s^{-1}}$
Bottom drag coefficient	$r_{drag} = 10^{-7}\ \mathrm{s^{-1}}$

Lateral momentum diffusivity	$A_h = 2 \cdot 10^{-6} \cdot (\frac{L_x}{n_x})^4$
Dissipation rate for large-scale motions	$r_{large} = 2 \cdot 10^{-6} \cdot (\frac{2\pi}{L_y})^2$
Time step	$dt = 300$ s
Duration	$T = 200$ days
Output frequency	$\omega_{out} = 16$ cycles/day
Layer thickness	$H_1 = 1000$ m $H_2 = 3000$ m

The system is doubly periodic and at $t = 0$ the wind stress is turned on gradually (as discussed in section 2.1.2). We then investigate the response of this initially motionless stratified fluid to the wind stress when the entire system is stable in time (Figure 2.5). Time-averaged values of kinetic energy calculated from new and standard methods are more or less the same.

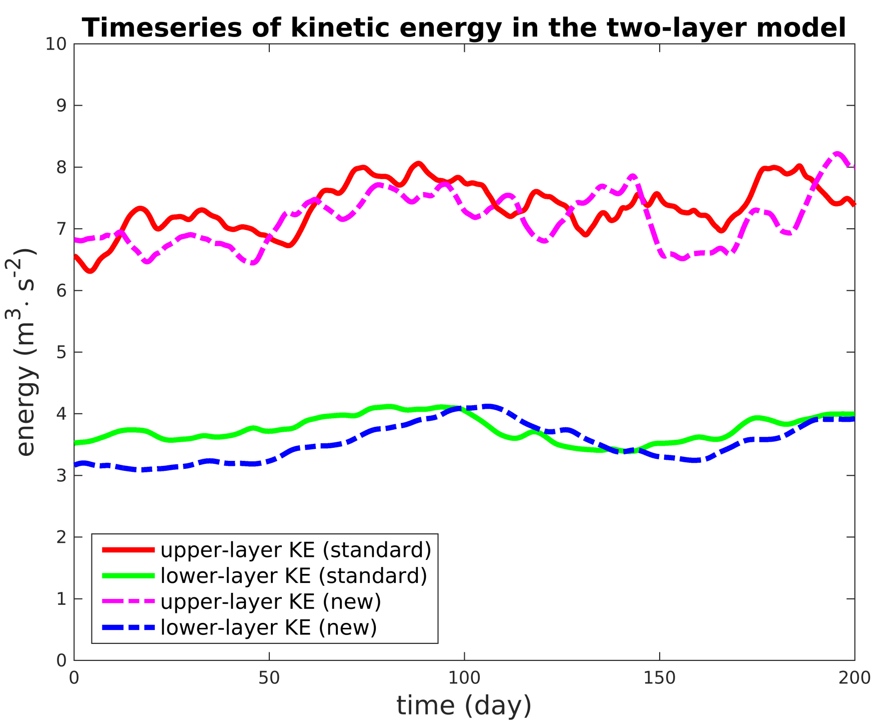

Figure 2.5 Timeseries of domain-averaged kinetic energy of both layers using standard and new methods

Chapter 3

Results

We will first present results for a reference simulation using standard forcing (described as the standard method previously). The reference simulation is chosen so as to produce a flow with Rossby numbers on the order of 0.1. While this is perhaps small relative to energetic currents such as the Gulf Stream or Kuroshio, it respects the small Rossby number approximation typically assumed in studies evoking Ekman theory. We will later be interested to see how our two-layer model forced using an assumed Ekman layer differs from the standard case. In other words, different responses of the interior ocean to standard and new forcing methods mentioned in early sections are displayed and compared. Because such differences are likely to vary with scale and between geostrophic and ageostrophic parts of the flow, we will be particularly interested in looking at frequency and wavenumber spectra, as well as in viewing the geostrophic and ageostrophic parts of the flow separately.

3.1 Reference case: a standard two-layer system forced by steady wind stress

First, we conduct a reference simulation in which a steady zonal wind stress is applied to the standard two-layer shallow water model. Figure 3.1 plots snapshots of various upper-layer fields to illustrate the flow regime of our reference simulation. Plotted are the two components of horizontal velocity, layer thickness and relative vorticity (normalized by planetary vorticity f). The flow pattern is dominated by large-scale zonal jets which are in the direction of wind stress, while the eddy components also account for a certain proportion. For example, the upper-layer velocities $|u_1| \sim 0.1 \text{ m s}^{-1}$ and the interface displacement $|\eta_2| \sim 200 \text{ m}$. The Rossby number $\varepsilon \sim 0.1$ is also consistent with both properties from the observed global-mean ocean and W&T experiments.

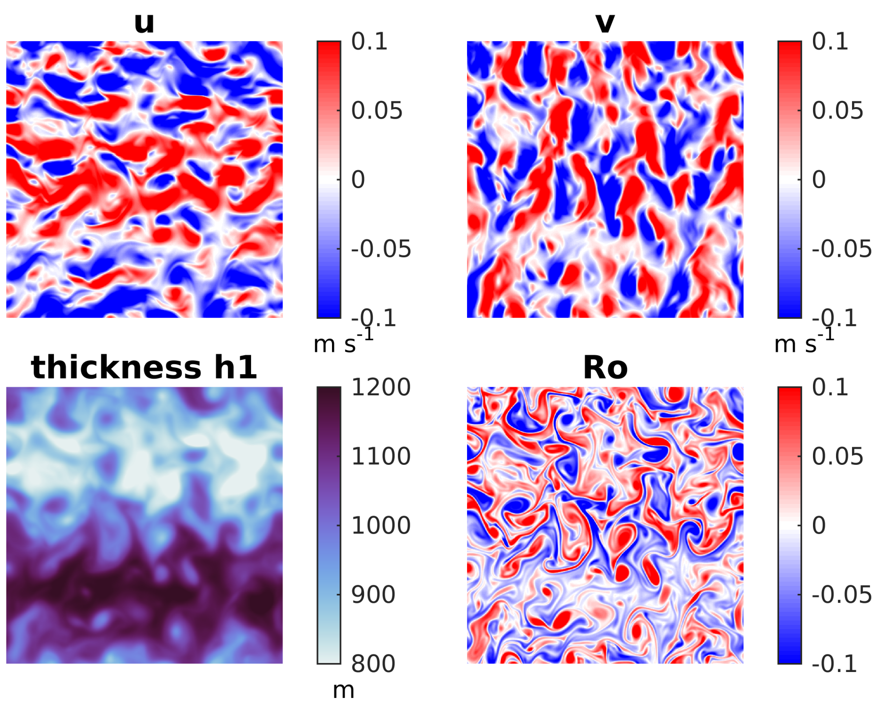

Figure 3.1 Snapshots for the field of the reference simulation. From left to right and from top to bottom, the subplots show upper-layer zonal velocity, meridional velocity, thickness, and Rossby number (relative vorticity normalized by f).

The upper panel in Figure 3.2 compares the upper-layer kinetic energy response with the one in lower layer. As is typical of wind-forced baroclinic flow, the lower layer is less energetic. This is true for all frequencies and wavenumbers, by comparing the red lines (upper-layer kinetic energy) with the blue lines (lower-layer kinetic energy) in Figure 3.3. One can also make such comparison in barotropic or baroclinic context (see Eqns (2.7) and (2.8)). The lower panel in Figure 3.2 shows baroclinic kinetic energy to dominate in our simulation. Again, this dominance is at all frequencies and all wavenumbers. The following parts will thus focus on the kinetic energy response of the baroclinic mode.

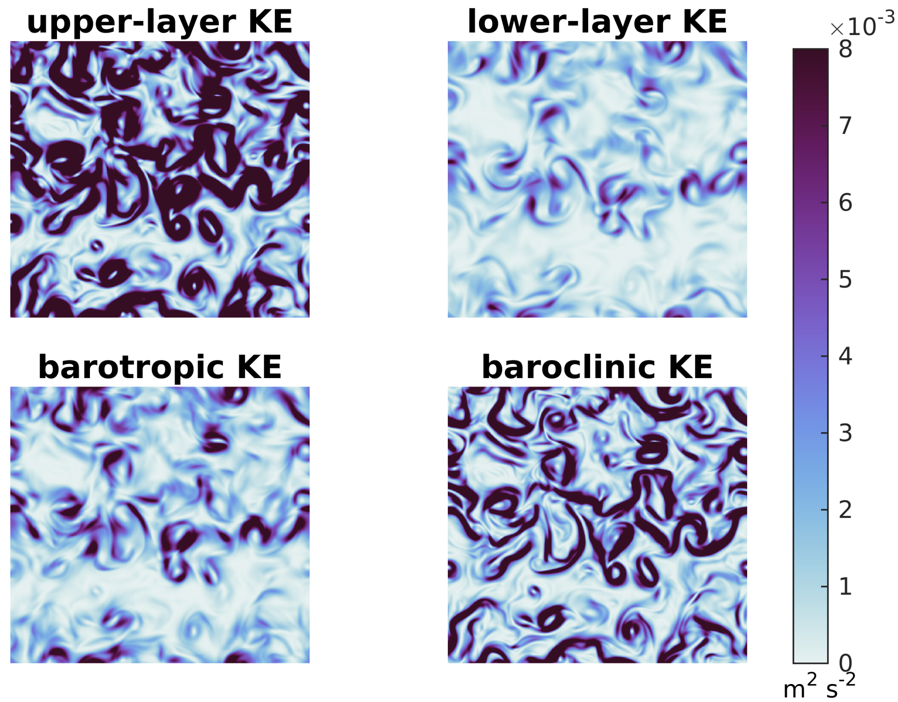

Figure 3.2 Snapshots for the field of the reference simulation. From left to right and from top to bottom, the subplots show upper-layer kinetic energy, lower-layer kinetic energy, barotropic kinetic energy and baroclinic kinetic energy.

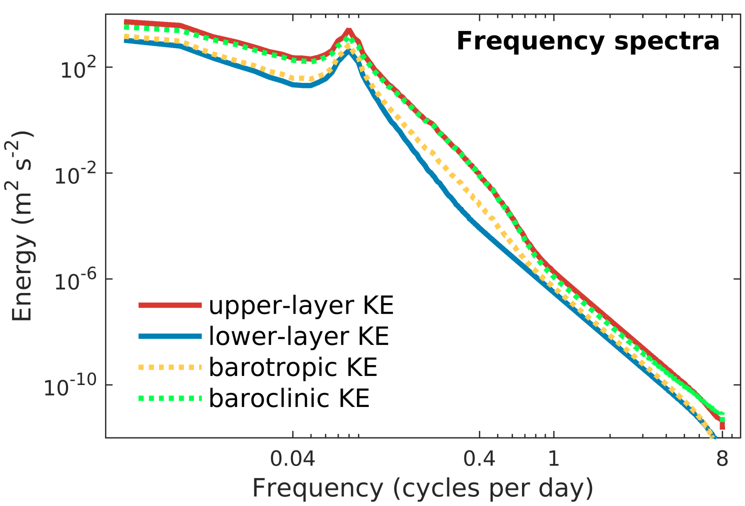

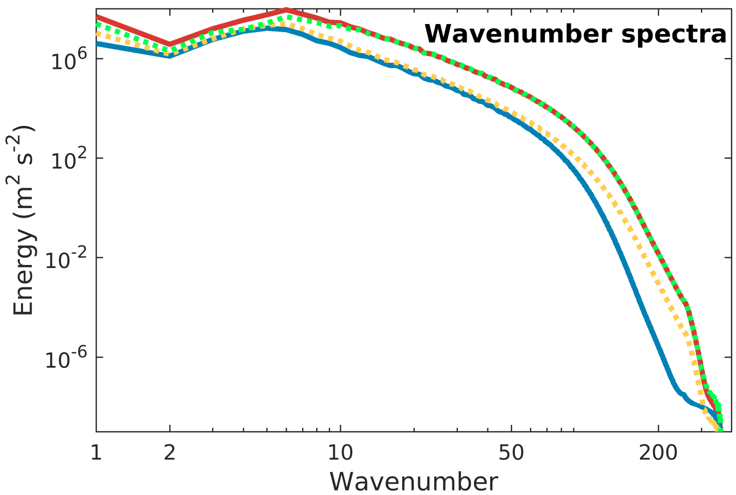

Figure 3.3 Frequency spectra and wavenumber spectra of upper-layer kinetic energy, lower-layer kinetic energy, barotropic kinetic energy and baroclinic kinetic energy in the reference simulation.

It is also of interest to decompose the flow into its geostrophic (QG) and ageostrophic (AG) components. Figure 3.4 does this for the baroclinic relative vorticity. As is evident from the figure, the flow is dominated by the geostrophic mode while variations in the ageostrophic component comprise only about 3% of the total.

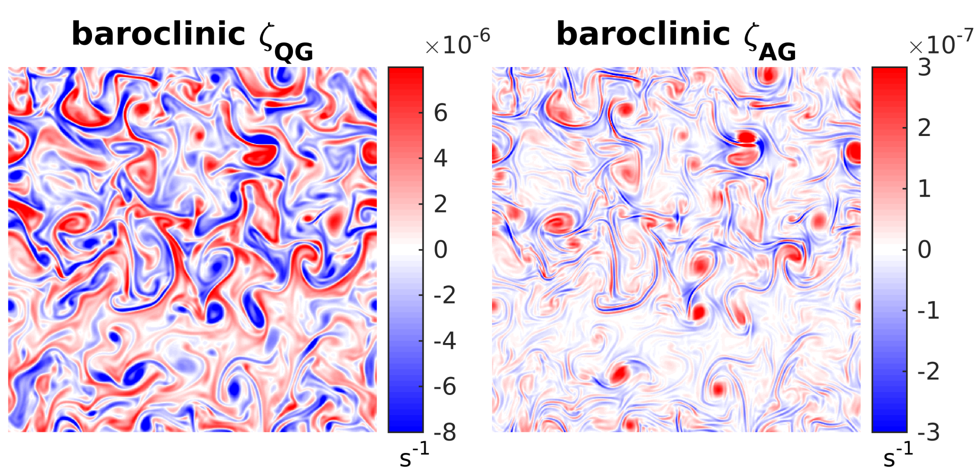

Figure 3.4 Snapshots for the baroclinic relative vorticity (QG and AG) fields of the reference simulation.

Consistent with Figure 3.4, the QG part of baroclinic kinetic energy is almost indistinguishable from the total baroclinic kinetic energy, with respect to both frequencies and wavenumbers (compare the red and blue curves in Figure 3.5). The sharp peak of the ageostrophic response at $\omega = 1$ corresponds to the Coriolis frequency, which is shown as the spikes of the AG frequency spectrum, but note that this peak remains near or below the (already weak) level of energy in the QG part of the spectrum at these frequencies. The low-frequency ageostrophic energy is considerably larger than the energy contained in the near-inertial peak and is likely related to Rossby number corrections to QG. Another noteworthy point from the wavenumber spectra is that the ratio of AG to QG kinetic energy increases with wavenumber. Nonetheless, QG motion continues to dominate up to the dissipation range (which begins near wavenumber 100).

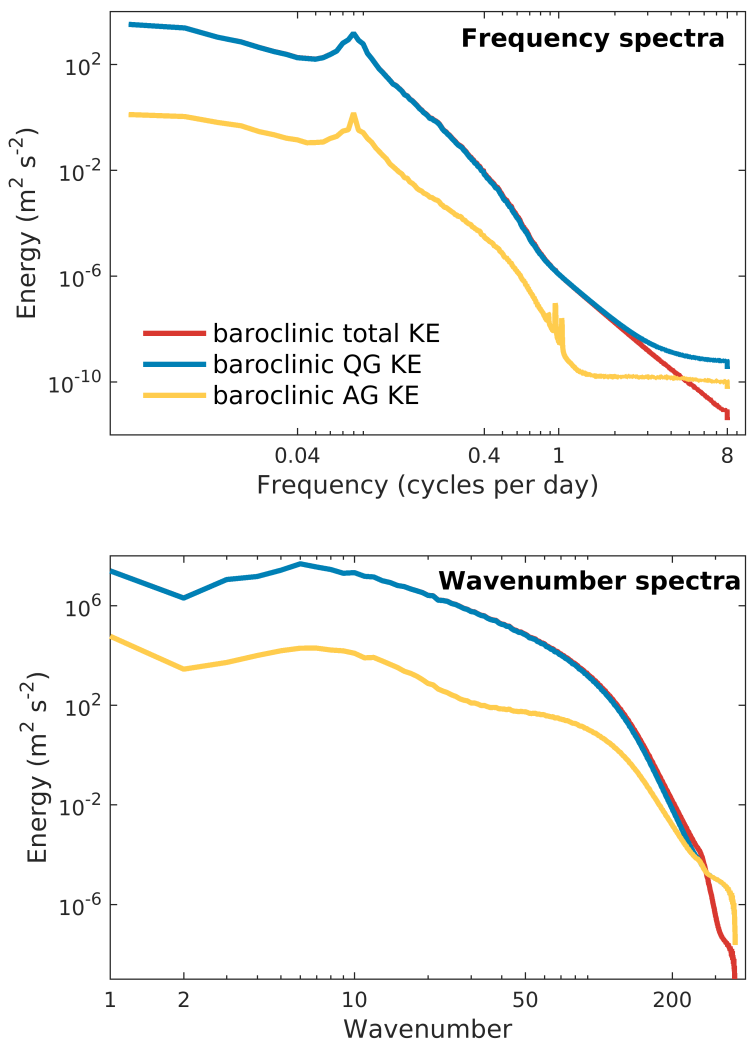

Figure 3.5 Frequency spectra and wavenumber spectra of total, QG and AG baroclinic kinetic energy in the reference simulation.

To conclude, the reference two-layer system is strongly baroclinic and in approximate quasigeostrophic balance. The ageostrophic component of this system is much smaller than the QG component, becoming comparable only at large wavenumbers.

3.2 Steady wind stress over an Ekman-interior coupled two-layer system

In this section, a comparison between an Ekman-interior coupled system and the reference system mentioned earlier will be discussed. Both simulations are forced by a steady wind stress. In other words, we compare two-layer shallow water simulations with new and standard methods, as described in section 2.2.4.

The major difference between these two methods is whether an explicit Ekman layer is applied as an intermediary between the wind forcing and the interior. We thus begin with a look of the temporal and spatial structures of the Ekman pumping (Figure 3.6). The wavenumber 1 forcing pattern (consistent with standard Ekman theory) is clearly dominant in both the snapshot and the wavenumber spectrum shown in the figure. Between wavenumbers 1 and 2, the spectrum falls off sharply, after which a positive slope is seen out to about wavenumber 100, which is associated with the wavelength of about 10 km. These small-scale structures are clearly evident in the snapshot and dominate the variability in the Ekman pumping. The frequency spectrum is relatively flat before tailing off around $\omega = 0.1\ \mathrm{cycle/day}$. There is a small peak at around $\omega = 0.02\ \mathrm{cycle/day}$ but we are unsure as to its origins and leave this for future study. To summarize, the Ekman pumping is dominated by the wavenumber 1 steady forcing given by the wind stress curl. Nonetheless, there is also a significant amount of higher-frequency and small-scale variability. It is therefore reasonable to anticipate the standard and new forcings will produce different results. Since the basic Ekman forcing is mainly from wavenumber 1, however, we anticipate that these differences will be subtle.

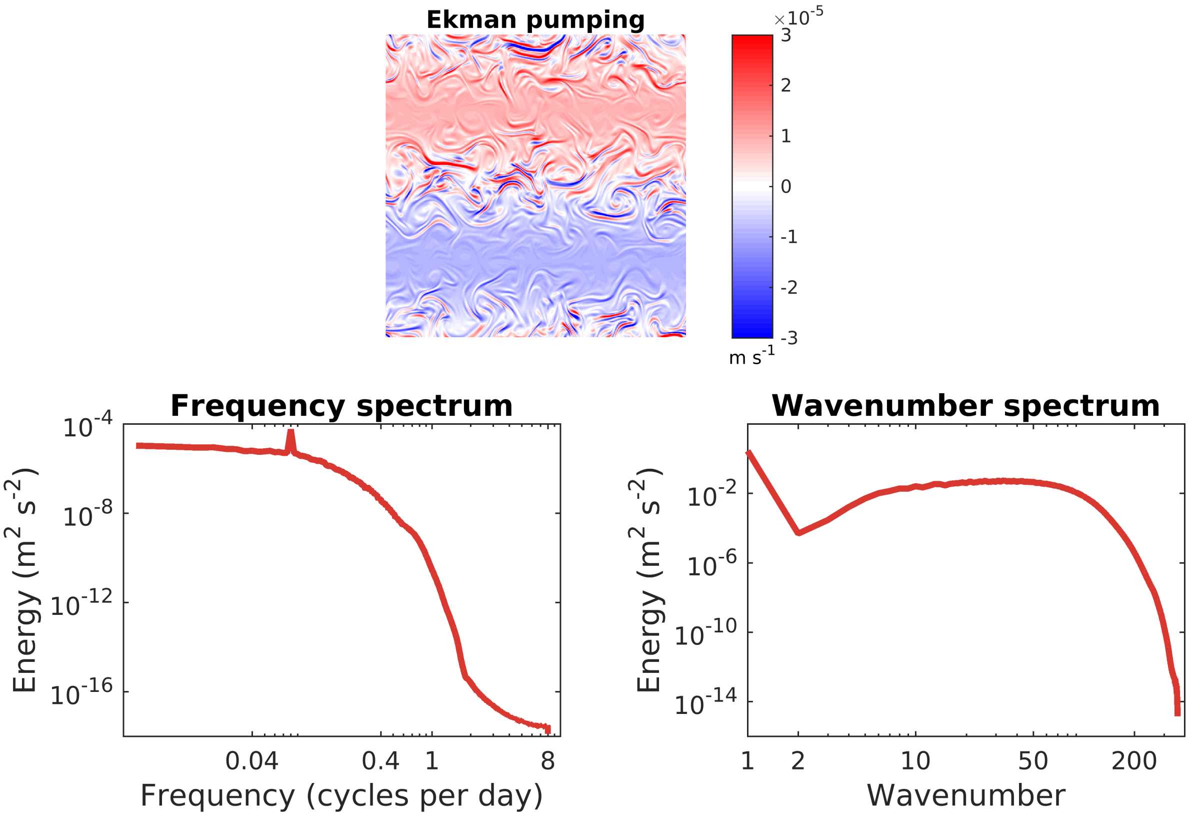

Figure 3.6 A snapshot, the frequency spectrum and wavenumber spectrum of Ekman pumping velocity in the Ekman-interior coupled system forced by steady wind.

Figure 3.7 and Figure 3.8 show frequency and wavenumber spectra of baroclinic kinetic energy using the new and standard forcings. Spectra with both forcing methods are nearly identical. This is true for both the QG and AG parts of the total flow. A small difference is that the system forced with new method contains more near-inertial baroclinic kinetic energy than the standard model (see Figure 3.7) while the wavenumber spectra do not show much difference between these two systems.

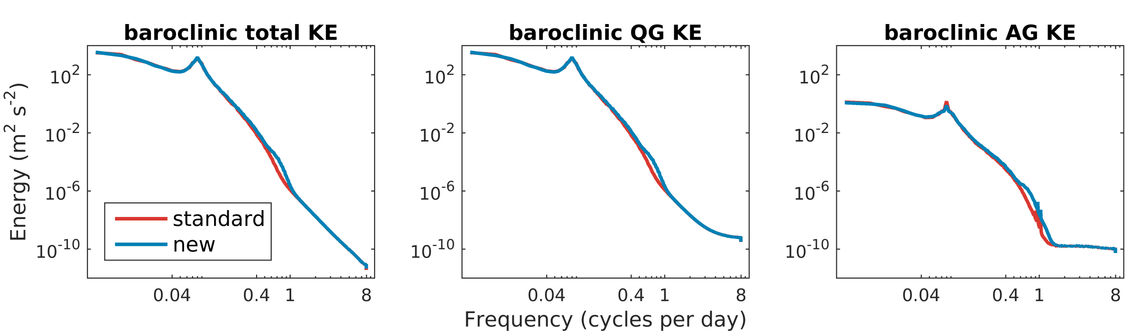

Figure 3.7 Frequency spectra of baroclinic kinetic energy in two-layer systems with new and standard methods. From top to bottom, the rows show total kinetic energy, quasigeostrophic kinetic energy and ageostrophic kinetic energy.

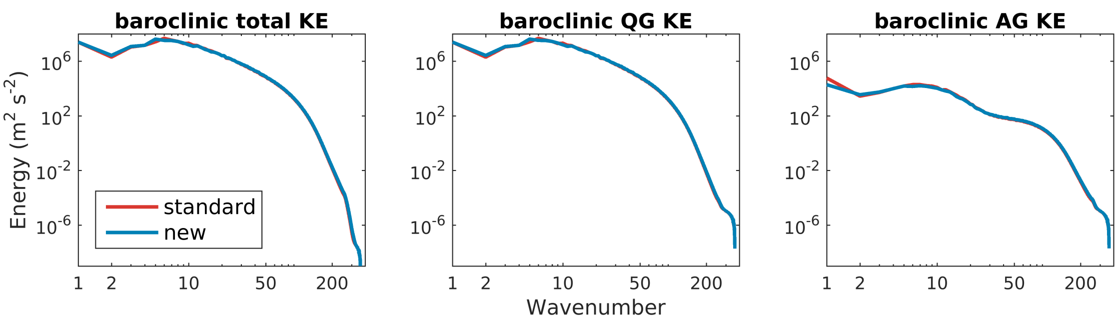

Figure 3.8 Wavenumber spectra of baroclinic kinetic energy in two-layer systems with new and standard methods. From top to bottom, the rows show total kinetic energy, quasigeostrophic kinetic energy and ageostrophic kinetic energy.

To summarize, the kinetic energy response of Ekman-interior coupled system is quite similar to the one from the reference or standard system (Figures 3.7-3.9). There are two or more possible explanations associated with the similarity. From the wavenumber spectrum in Figure 3.6, the Ekman pumping forcing for the interior ocean in our new system is mostly at wavenumber 1. Hence, the high-frequency small-scale Ekman pumping is inefficient at forcing interior flow. Later we will check this possibility by identify the spatial scale of high-frequency components in the kinetic energy response of our new Ekman-interior coupled system. If the near-inertial components are associated with scales relatively large compared to the deformation radius, then the hypothesis above is possibly right. Another possibility is that the standard method forces the interior in a similar manner because the forcing term in associated momentum equations is also time-dependent (containing high frequencies), e.g., the right hand side in Eqn (2.20) is $\frac{\boldsymbol{\tau}}{h_1}$ where h_1 is dependent on time. Using potential vorticity equations of these two systems might be an alternative way to compare forcings and responses of the two methods but we will leave the analysis of potential vorticity to future studies.

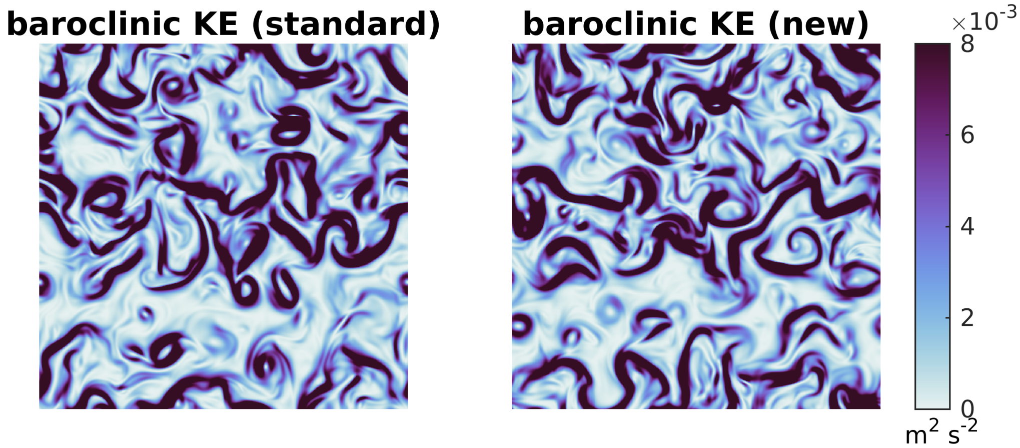

Figure 3.9 Snapshots for the baroclinic total kinetic energy fields of standard and new systems.

Figure 3.10 illustrates the complexity of the flow, which is characterized by eddies and filaments. Clearly for such a flow, using the method proposed by Wenegrat and Thomas to calculate the flow-dependent Ekman pumping field would be intractable. For example, even with simple cyclonic or anticyclonic structures shown in the lower panel of Figure 3.10, it is difficult to apply W&T method to calculate the pumping velocities since the structures are irregular. Compared with their method, our calculation is more applicable to turbulent flow field, however, our method of using an explicit representation of Ekman pumping in two-layer model made little difference in terms of interior energy response, compared to the standard two-layer shallow water model. We speculate previously that this lack of difference might be related to i) the relatively low Rossby number of the flows simulated and ii) the absence of fast time scale wind forcing (and this conjecture is similar to the previous speculation that forcing term in standard model is also time-dependent). In the next section, we explore the latter possibility by adding a time variable component to the wind stress.

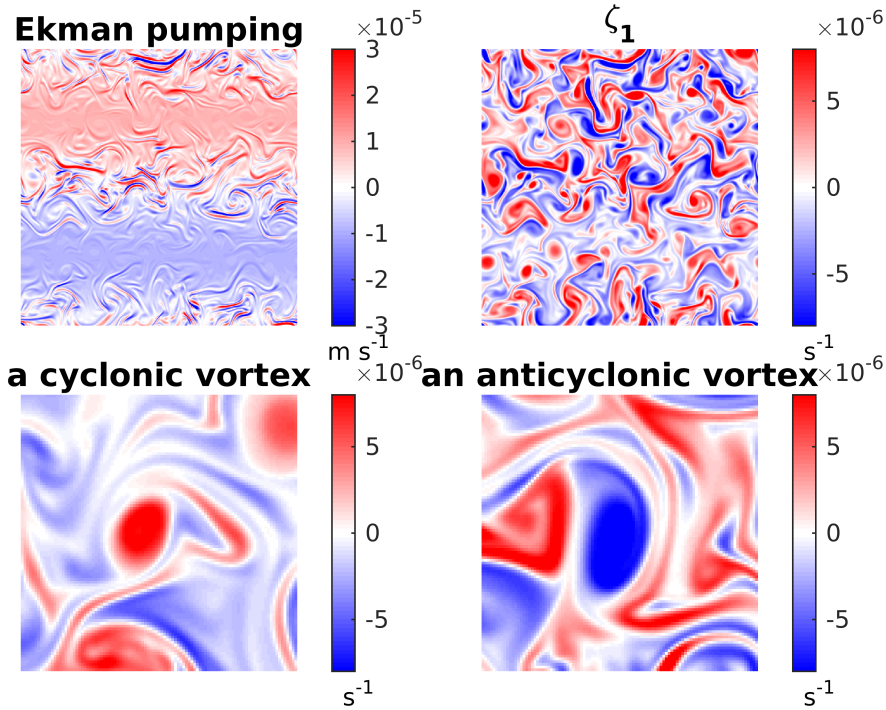

Figure 3.10 Snapshots for the Ekman-interior coupled system forced by steady wind stress. From top to bottom and from left to right, plots show Ekman pumping velocity, upper-layer relative vorticity, an enlargement of the upper-layer relative vorticity field to illustrate a typical cyclonic vortex and an anticyclonic vortex.

3.3 Impacts of unsteady wind

Any two-layer system described before this section was forced by a steady westerly wind stress varying sinusoidally in y-direction as described by (2.24a), with the maximum wind stress $\tau_0 = 2 \cdot 10^{-4}\ \mathrm{m}^2\ \mathrm{s}^{-2}$. In this section, a high-frequency component of the wind forcing is introduced so as to test whether the Ekman-interior coupled system is different from the reference system in regard to energy response. The modified wind stress at any time point is then described as

$$\tau^x = \tau_0 \cos\left(\frac{2\pi y}{L_y}\right) + \tau_1 \sin\left(ft\right) \tag{3.1}$$

where $\tau_1 = 10^{-5}\ \mathrm{m}^2\ \mathrm{s}^{-2}$ and t is time. Hence, our new wind stress includes a steady part which has the same value as the one described in section 3.1 and 3.2, but also an unsteady component which is uniform in space.

Figure 3.11 and 3.12 give an impression of how different the Ekman forcing of new wind stress is from the steady-wind case, even though the time-dependent component of τ^x is relatively small compared with the stationary component ($\frac{\tau_1}{\tau_0} = 0.05$). The near-inertial Ekman forcing for the unsteady wind case is considerable; it is larger than low-frequency components, as can be seen from the blue frequency spectrum in Figure 3.12. We might then expect a similar difference in response of our two-layer system to the new Ekman pumping, which is assumed to contain a large amount of high frequencies; however, as shown below this is not the case. That is, the major differences are limited to the high-frequency end of the spectrum (as one might expect) and high-frequency energy remains small compared to its low-frequency counterpart.

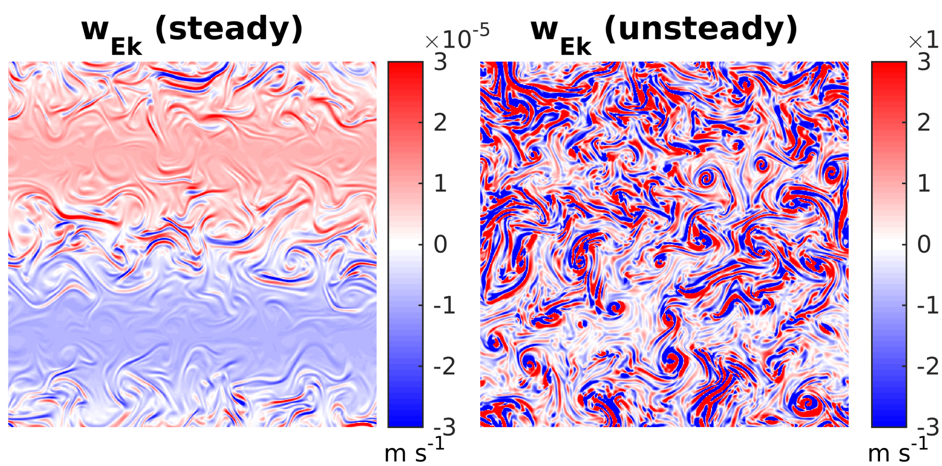

Figure 3.11 Snapshots for the Ekman pumping velocities of the steady-wind and unsteady-wind cases separately (of the Ekman-interior coupled model).

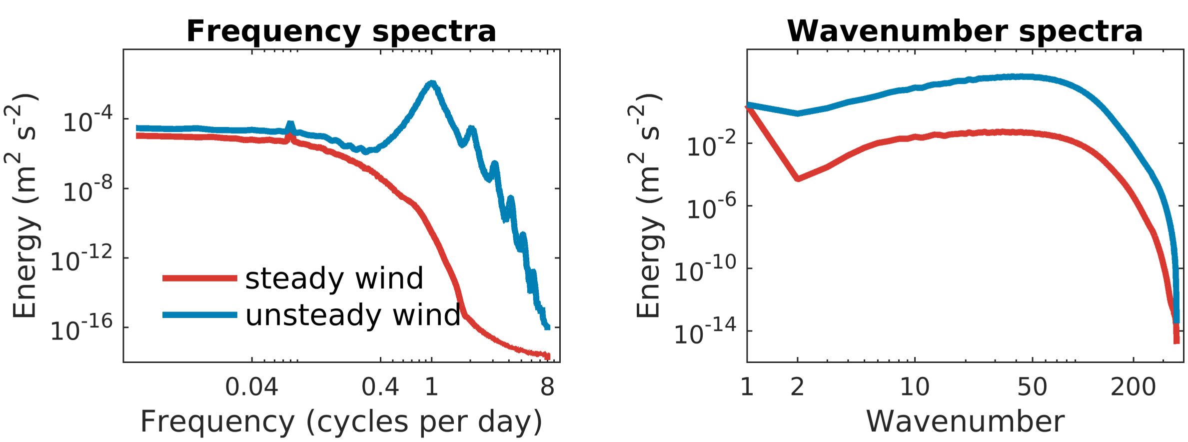

Figure 3.12 Frequency spectra and wavenumber spectra of w_{Ek} of the steady-wind and unsteady-wind cases separately (of the Ekman-interior coupled model).

Figure 3.13 compares four simulations together: standard or new forcing mechanisms with steady or unsteady wind. The four frequency spectra of the total baroclinic kinetic energy coincide almost perfectly at low frequencies, but diverge significantly at near-inertial and higher frequencies (see Figure 3.13 upper left). The decomposition of kinetic energy into QG and AG parts also shows similar characteristics between new and standard regimes forced by unsteady wind in terms of frequency analysis. That is, the high-frequency peak is significantly wider in the Ekman-interior coupled system than the reference system. Additionally, the QG part of this high-frequency peak is much larger for the simulation using the new forcing method (see green and yellow curves in Figure 3.13 middle left panel). Conversely, the four wavenumber spectra of total or QG baroclinic kinetic energy show remarkable agreement at all wavenumbers. A comparison between the frequency spectrum and the wavenumber spectrum of the ageostrophic kinetic energy seems to show that this high-frequency difference between the two mechanisms spreads over a broad range of spatial scales.

Another interesting point to note is the comparison between QG and AG components of the Ekman-interior coupled system forced by unsteady wind. Most people would associate near-inertial motion with the AG modes, however, QG modes also contribute to high-frequency energy response (e.g., compare the two green curves of QG and AG frequency spectra in Figure 3.13).

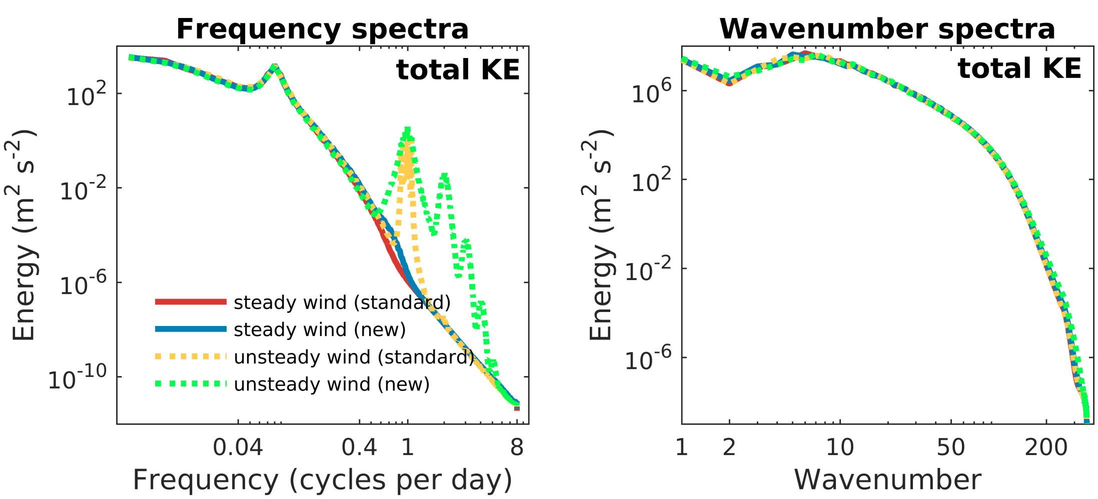

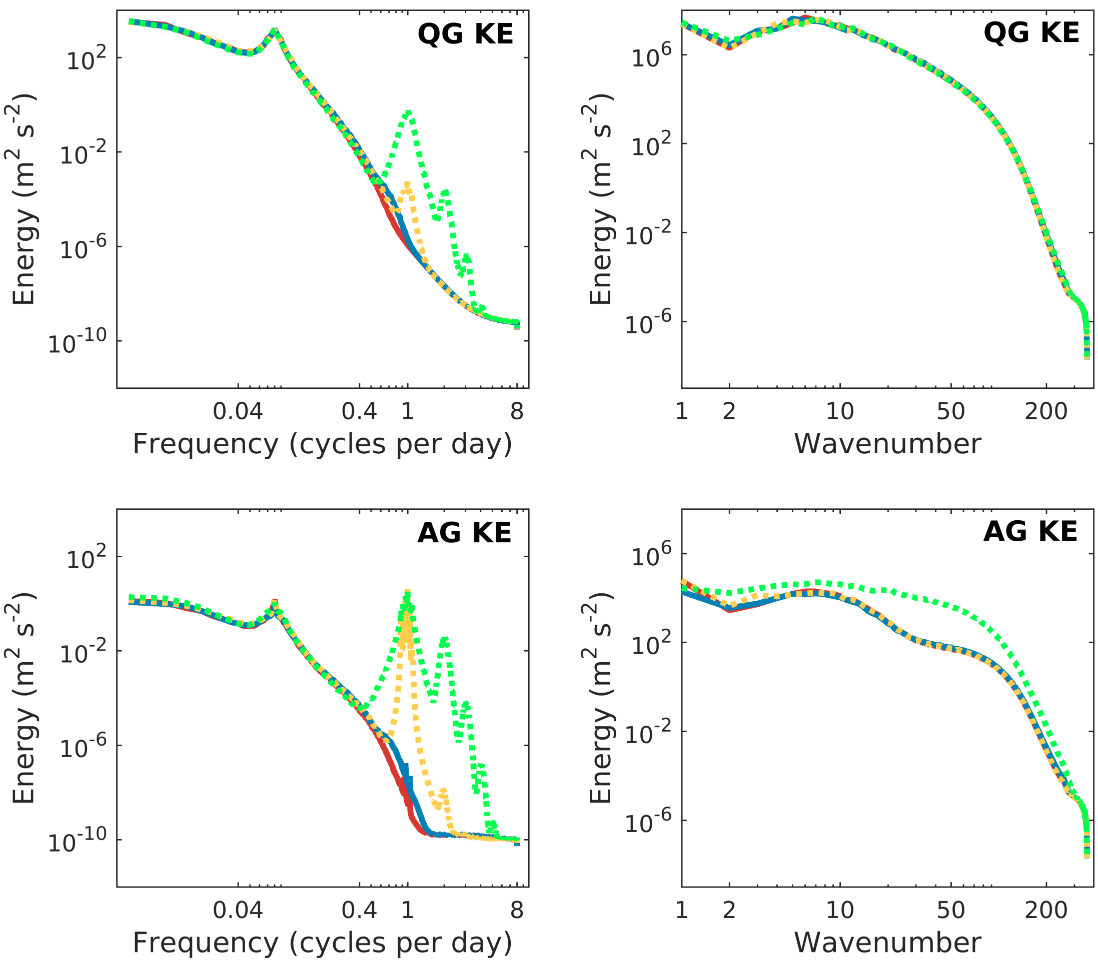

Figure 3.13 Frequency spectra and wavenumber spectra of baroclinic kinetic energy in two-layer systems with new and standard methods. From top to bottom, the rows show total kinetic energy, quasigeostrophic kinetic energy and ageostrophic kinetic energy.

Focusing on AG modes (the bottom panel in Figure 3.13), it is apparent that there are sizable differences in high-frequency energy in response to the two methods of forcing and these differences are visible at almost all wavenumbers. The high-frequency QG modes (the middle panel in Figure 3.13), on the other hand constitute a much smaller fraction of the total QG energy. As such, it does not significantly affect the wavenumber spectrum, which is dominated by the slow modes. To get a better understanding of the spatial structure of the fast QG and AG modes, we now separate high-frequency components of the kinetic energy from the total (Figure 3.14). To isolate the high frequencies, we subtract instantaneous values from a two-day running mean, which we consider to be the low-frequency part of the flow. It is apparent that the difference of high frequencies between these two methods is almost at each wavenumber. And the main difference is in the AG modes while QG modes show difference at small to moderate wavenumbers.

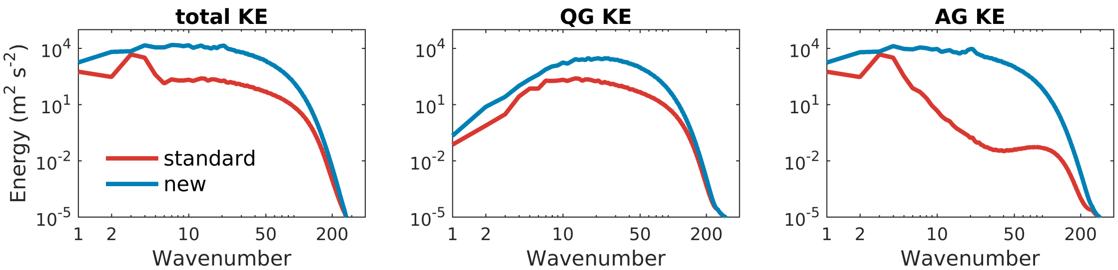

Figure 3.14 Wavenumber spectra of baroclinic high-frequency kinetic energy for the unsteady wind case: total (left), QG (middle) and AG (right).

To conclude, a first comparison between the standard and new cases where both systems are forced by steady wind shows little difference. Even the weak ageostrophic part of the flow shows spectra that essentially agree between the two cases. This lack of difference is consistent with the Ekman pumping being dominated by its steady wavenumber 1 component (as is the wind forcing applied directly to the momentum equation in the standard model). We then turn to a case where the wind stress also includes high frequencies. In this case, the Ekman pumping inferred using our new forcing method not only contains a large amount of energy at near-inertial frequencies, but also is skewed towards relatively high wavenumbers. In this case the two models show significantly different responses. These differences are largely provided by the ageostrophic modes. That is, the larger horizontal scales, at which geostrophy dominates, remain insensitive to the method of forcing. This is consistent with quasigeostrophic theory, for which forcing in the momentum or mass equations is equivalent.

Chapter 4

Conclusions and discussions

The influence of relative vorticity on Ekman pumping has long been recognized and theoretically improved. However, all previous theories assume the Ekman flow to be determined by instantaneous values of the wind stress and surface velocities. That is, both the winds and the surface currents are assumed to vary on time scales slow compared to the time needed to establish the Ekman balance. Explicit time dependence in the Ekman equations is thus ignored. In order to further apply the flow-dependent Ekman theory to complicated turbulent fields, we add time dependence to the associated Ekman equations. By doing so, it becomes possible to solve for the Ekman transport without the need to perform line integrals along complex streamlines, which greatly simplifies calculation.

In order to validate our time-dependent Ekman layer, we first reproduce Wenegrat and Thomas's results for a balanced vortex, however, our method also introduces a strong near-inertial component to the Ekman pumping, except in cases where the wind stress is ramped up very slowly. We next couple our new flow-dependent Ekman layer to a two-layer shallow water model and compare it with a standard wind-driven two-layer regime. This comparison makes up the core part of the thesis. The standard regime forced by a steady wind stress is also set as a reference simulation and each simulation resulting from other forcing possibilities is compared with the reference.

The standard model and the Ekman-interior coupled model forced by steady wind stress give tiny difference between the two regimes in regard to the baroclinic kinetic energy response, even though Ekman pumping forcing in the coupled system has a relatively large proportion of high frequencies. We then add unsteady components which oscillate at Coriolis frequency to the steady wind stress. In this case the two models show significantly different responses, especially in near-inertial frequency range of the ageostrophic kinetic energy. And later we find this high-frequency difference is related to all wavenumbers.

To further compare the difference between new and standard forcing regimes, it is also possible to turn to equations of the upper-layer potential vorticity (PV).

Taking curl of Eqn (2.20) and combine it with Eqn (2.21), one can obtain the upper-layer PV equation of a standard system. Using similar derivation method with Eqns (2.22) and (2.23), the upper-layer PV equation for the coupled system is also determined.

$$\frac{D}{Dt}\left(\frac{f+\zeta_1}{h_1}\right)=\frac{1}{h_1}\left(\nabla\times\frac{\boldsymbol{\tau}}{h_1}\right) \tag{4.1}$$

$$\frac{D}{Dt}\left(\frac{f+\zeta_1}{h_1}\right)=\frac{(f+\zeta_1)\cdot w_{Ek}}{h_1^2} \tag{4.2}$$

Eqns (4.1) and (4.2) are then the upper-layer PV equations for standard and new forcing methods. The upper-layer PV is defined as $q_1=\frac{f+\zeta_1}{h_1}$, which can be regarded as the vortical response of upper layer while the right hand side of above equations can be thought of as forcing which helps to determine the PV response of each method. Thus, we can define the right hand side of (4.1) and (4.2) to be PV forcings for each method. Comparing these two systems from the perspective of PV is then an alternative way to understand the difference and this will be left to future work.

We also mentioned previously that the background flow simulated here has low Rossby numbers. Another possible future work is therefore to try a set of background flows with different Rossby numbers. With different spatial scales of background flow, the interaction between Ekman dynamics and the interior might also result in surprising responses.

Another important improvement of this flow-dependent Ekman dynamics is to think about the nonlinearity. Look back on Eqn (2.1) and we know that in our flow-dependent Ekman equation the nonlinear Ekman self-advection term, $(\boldsymbol{u}_{Ek}\cdot\nabla)\boldsymbol{u}_{Ek}$ (the fourth term in Eqn (2.1)), is ignored. It is reasonable for the scale assumption where $\varepsilon_{Ek}\ll 1$ and $\varepsilon<1$. However, if the Ekman flow and the background flow are comparable to each other in terms of their spatial structures, it is then necessary to add this term back to our Ekman equation. Then, Eqn (2.3) includes another term, the vertical integral of the Ekman self-advection term in Eqn (2.1). However, calculating this new term in Eqn (2.3) at least needs to define an Ekman layer thickness in the model and more parameterization methods might be introduced for further study.

Bibliography

1. Chelton, D. B., Schlax, M. G., and Samelson, R. M. (2011). Global observations of nonlinear mesoscale eddies. *Progress in Oceanography*, 91, 167-216. https://doi.org/10.1016/j.pocean.2011.01.002
2. Dewar, W., and Flierl, G. (1987). Some effects of the wind on rings. *Journal of Physical Oceanography*, 17, 1653-1667. https://doi.org/10.1175/1520-0485(1987)017<1653:SEOTWO>2.0.CO;2
3. Duhaut, T. H., and Straub, D. N. (2006). Wind stress dependence on ocean surface velocity: implications for mechanical energy input to ocean circulation. *Journal of Physical Oceanography*, 36, 202-211. https://doi.org/10.1175/JPO2842.1
4. Ekman, V. (1905). On the influence of the Earth's rotation on ocean-currents. *Arkiv for Matematik, Astronomi och Fysik*, 2, 1-53.
5. Gaube, P., Chelton, D. B., Samelson, R. M., Schlax, M. G., and O'Neill, L. W. (2015). Satellite observations of mesoscale eddy-induced Ekman pumping. *Journal of Physical Oceanography*, 45, 104-132. https://doi.org/10.1175/JPO-D-14-0032.1
6. Gaube, P., and McGillicuddy, D. J. (2017). The influence of Gulf Stream eddies and meanders on near-surface chlorophyll. *Deep Sea Research Part I: Oceanographic Research Papers*, 122, 1-16. https://doi.org/10.1016/j.dsr.2017.02.006
7. Gill, A. E. (1982). Atmosphere-Ocean Dynamics. *Academic press*.
8. Hallberg, R., and Gnanadesikan, A. (2001). An exploration of the role of transient eddies in determining the transport of a zonally reentrant current. *Journal of Physical Oceanography*, 31, 3312-3330. https://doi.org/10.1175/1520-0485(2001)031<3312:AEOTRO>2.0.CO;2
9. Liu, F., and Tang, S. (2018). Influence of the interaction between typhoons and oceanic mesoscale eddies on phytoplankton blooms. *Journal of Geophysical Research: Oceans*, 123:4, 2795-2794. https://doi.org/10.1029/2017jC013225
10. Liu, M., and Rossby, T. (1993). Observations of the velocity and vorticity structure of Gulf Stream meanders. *Journal of Physical Oceanography*, 23, 329-345. https://doi.org/10.1175/1520-0485(1993)023<0329:OOTVAV>2.0.CO;2
11. Mahadevan, A. (2016). The impact of submesoscale physics on primary productivity of plankton. *Annual Review of Marine Science*, 8,161-184. https://doi.org/10.1146/annurev-marine-010814-015912
12. Marshall, J., and Plumb, A. (2008). Atmosphere, ocean, and climate dynamics: an introductory text. *Elsevier*.
13. Niiler, P. P. (1969). On the Ekman divergence in an oceanic jet. *Journal of Geophysical Research*, 74, 7048-7052. https://doi.org/10.1029/JC074i028p07048
14. Pedlosky, J. (2008). On the weakly nonlinear Ekman layer: Thickness and flux. *Journal of Physical Oceanography*, 38, 1334-1339. https://doi.org/10.1175/2007JPO3830.1
15. Risien, C. M., and Chelton, D. B. (2008). A global climatology of surface wind and wind stress fields from eight years of QuikSCAT scatterometer data. *Journal of Physical Oceanography*, 38, 2379-2413. https://doi.org/10.1175/2008JPO3881.1
16. Salmon, R. (1998). Lectures on Geophysical fluid dynamics. *Oxford University Press*.

17. Stern, M. E. (1965). Interaction of a uniform wind stress with a geostrophic vortex. *Deep Sea Research and Oceanographic Abstracts*, 12, 355-367. https://doi.org/10.1016/0011-7471(65)90007-0
18. Sverdrup, H. U. (1947). Wind-driven currents in a baroclinic ocean; with application to the equatorial currents of the eastern Pacific. *Proceedings of the national academy of sciences of the United States of America*, 33, 318-326.
19. Thomas, L. N., and Rhines, P.B. (2002). Nonlinear stratified spin-up. *Journal of Fluid Mechanics*, 473, 211-244. https://doi.org/10.1017/S0022112002002367
20. Trenberth, K. E., Large, W. G., and Olson, J. G. (1989). The effective drag coefficient for calculating wind stress over the ocean. *Journal of Climate*, 2, 1507-1516. https://doi.org/10.1175/1520-0442(1989)002<1507:TEDCFE>2.0.CO;2
21. Wenegrat, J. O., and McPhaden, M. J. (2016). A simple analytical model of the diurnal Ekman layer. *Journal of Physical Oceanography*, 46, 2877-2894. https://doi.org/10.1175/JPO-D-16-0031.1
22. Wenegrat, J. O., and Thomas, L. N. (2017). Ekman transport in balanced currents with curvature. *Journal of Physical Oceanography*, 47, 1189-1203. https://doi.org/10.1175/JPO-D-16-0239.1
23. Vallis, G. K. (2006). Atmospheric and Oceanic Fluid Dynamics: Fundamentals and Large-Scale Circulation. *Cambridge University Press*.
24. Zhai, X., Johoson, H. L., Marshall, D. P., and Wunsch, C. (2012). On the wind power input to the ocean general circulation. *Journal of Physical Oceanography*, 42, 1357-1365. https://doi.org/10.1175/JPO-D-12-09.1